Johann-Wolfgang Goethe Universität Frankfurt

Institut für Kernphysik Frankfurt

Masterthesis

Electron identification with a likelihood method and measurements of di-electrons for the CBM-TRD

eingereicht von: Etienne Bechtel

eingereicht am: 23.03.2017

Erstgutachter: Prof. Christoph Blume

Zweitgutachter: Prof. Tetyana Galatyuk

Contents

List of Figures

1 Motivation

Curiosity and the will to understand the world around us was always something that influenced humanity as a whole. Combined with the ability to think logically, this is one of the main reasons for our technology and society nowadays. But even with all the knowledge we acquired so far, there are still huge empty spots in our net of knowledge. Modern science is trying to fill these empty spots. With the science of high energy physics we want to address one of the most fundamental questions we could ask, which is the question of the beginning of the universe and the interactions which formed our universe today. Starting with the so-called *big bang* our known universe developed from a singularity under the influence of the fundamental interactions. These interactions are the gravitation, the electromagnetic, the weak and the strong interaction. A task of high energy physics is to investigate the behaviour of strongly interacting matter as it was in the early stage of the universe and to map out its phase diagram.
The CBM experiment is supposed to have a deeper look into the region of high net-baryon densities and to search for deconfinement and chiral phase transitions. It is designed to operate at very high event rates and will be able to investigate rare diagnostic probes.

This work is supposed to make a contribution to the basic software needs for such investigations which is a robust and high performing particle identification. The idea is to implement and optimize a likelihood method for particle identification for the CBM ***T****ransition* ***R****adiation* ***D****etector* (TRD). It is also designated to have a look in the corresponding performance with attention to di-electron signals.

2 Theory

2.1 The Standard Model

The history of high-energy physics starts with the discoveries of radioactivity by Becquerel (1896) and of the electron by Thomson (1897). Thomson also developed his model of the atom with a continuous mass distribution and homogeneously distributed electrons [tho17]. This model got disproven by Rutherford in 1911 who used α particles to shoot them into a gold foil and then observed the angular distribution of the scattered particles. He saw scattering angles that could not be explained by the continuous mass distribution of the Thomson model. Instead, a solid core inside the atom orbited by light electrons could explain the observation. This conclusion lead to what we call the Rutherford atomic model which is still taught in schools. In 1917 Rutherford discovered the proton and, together with the neutron which was found by Chadwick in 1932, the circle seemed to be complete for some scientists. But there was also the fact that the Dirac equation predicted the existence of antiparticles. Starting with the discovery of the pion in 1946 suddenly a large number of new particles was found which enforced the need for a new model [rut17].

In 1964 Gell-Mann postulated the existence of quarks as new fundamental particles. The quark-model was born. The quarks he postulated should have a half-integer spin and a fraction of one as electric charge. Initially he spoke about three different quark flavours which was later extended by three additional flavours.

The elementary particles which form all visible matter and the forces between them are summarized in the standard model of particle physics. It consists out of [sta17]:

- 6 Quarks
- 6 Leptons
- 5 Bosons

The quarks and the leptons are categorized in families as one can see in the columns of Fig. 2.1. The quarks and leptons are fermions with a half-integer

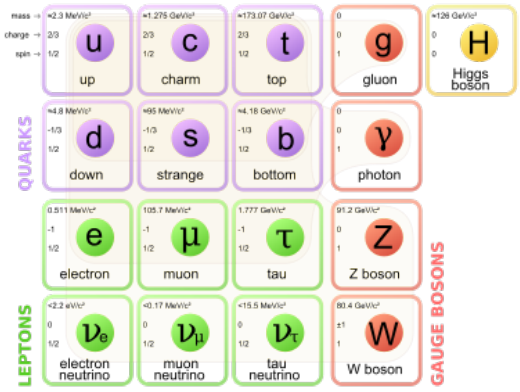

Figure 2.1: The standard model of particle physics showing the different generations of quarks and leptons as well as the exchange particles of the four fundamental interactions and the higgs boson [Picd].

spin. The five particles on the right side are bosons with an integer spin. The fermions on the left side are divided into the mentioned quarks (upper half) and leptons (lower half). Leptons are fundamental particles and they exist unbound. On the other hand the quarks are normally bound into hadrons which further can be separated into baryons and mesons.
The quarks all carry a baryon number of $B = \frac{1}{3}$ and the antiquarks carry B=-$\frac{1}{3}$. In a hadron the baryon numbers add up and if the result is $B = \pm 1$ we are speaking of baryons and if the result is $B = 0$ it is called a meson [sta17]. For the leptons the categorisation in families is very important since the standard model includes the so called *lepton number conservation*. Every lepton carries a lepton number of +1 and every antilepton a lepton number of -1. These lepton numbers are defined for every family separately (L_e, L_μ, L_τ), which therefore determines their possible decay modes.

On the right hand side of Fig. 2.1 one can see the bosons of the standard model which are the exchange particles for the three fundamental forces included in the standard model. The included forces are the electromagnetic force with the photon (γ) as exchange particle, the weak interaction with W and Z bosons and the strong interaction with the *gluon* (g). These exchange particles couple to the charges of the different interactions, respectively the electric charge (EM-interaction), the weak isospin (weak interaction) and the colour (strong interaction). The gravitation is not part of the standard model. This fact is one of the concerns of physicists, since the standard model is intended to get replaced by an even more complete theory that includes the gravitation and may be able to address other difficult questions like the

	Strength	Range	Time scale (s)	Crosssection	Field Quanta
Strong	1	~ Fm	$< 10^{-22}$	$< 10^{-30}$ m²	Gluons
Weak	10^{-5}	10^{-3} Fm	10^{-8}	10^{-44} m²	$W^{\pm}$,Z^0
EM	1/137	∞	10^{-20}	10^{-33} m²	Photon
Gravitational	10^{-38}	∞			Graviton?

Figure 2.2: Different parameters of the four fundamental forces in comparison. Listed are the relative strength between the forces, their range, their time scale, their cross sections and their exchange particles. [Pica]

asymmetry between matter and antimatter as well. This was not possible yet and the standard model allows for a very good description of all observations.

The mass of the exchange particles determines the range of the interaction. Since our model is speaking about virtual exchange particles they are just produced for a limited amount of time depending on their mass. This is related to the uncertainty principle. Especially the large masses of the $W^{\pm}$ and Z boson correspond to a short range of the weak interaction. In comparison, the photon has no mass and the EM-interaction therefore an infinite range. The gluon also has no mass but the strong interaction possesses a short range. This is due to the interactions
The masses itself are a result of the $Higgs - Boson$ which was found in 2012 at CERN or, more precisely, they are a result of the Higgs mechanism [ATL12]. A simple description of the Higgs mechanism is as a quantum field that exists everywhere in space. The field is coupled to all particles with an individual coupling constant and when the chiral symmetry breaks the particles get their masses.

2.2 The Strong Interaction

The strong interaction is responsible for building the hadrons and it is the primary force for the decays of particles, if allowed by conservation laws. The reason for this is that the strong interaction has a much larger coupling constant and therefore results in much shorter lifetimes for particles that can decay via the strong interaction (Fig. 2.2). The main reason for particles to decay via the weak interaction is that the strong interaction is not able to change quantum numbers like strangeness, which only the weak interaction can do [str17].

The charge of the strong interaction is the colour and the quantum field theory to describe this interaction is the ***Q**uantum **C**hromo **D**ynamics* (QCD), similar to the theory of the EM-interaction ***Q**uantum **E**lectro **D**ynamics* (QED). The colour of the strong interaction is defined as *red, green, blue, anti-red, anti-green* and *anti-blue*. Quarks carry a colour and antiquarks carry an anticolour. A big difference between the gluons and the photons is that gluons are able to interact with themselves, since they carry colour charge, while photons do not carry an electric charge.
There are eight different colour states for the gluons where six of those are a simple combination of a colour and an anticolour and two of are a superposition of colour and anticolour (Fig. 2.3). The superpositions result from the fundamental symmetry ($SU(3)_{colour}$) of QCD [str17].

Another very important property about the strong interaction is the so called *asymptotic freedom*. This phenomenon describes the fact that the coupling constant of the strong interaction between a quark and an antiquark has an energy dependency (Fig. 2.4).
The potential of a quark-antiquark pair is given by the formula:

$$V = -\frac{4}{3}\frac{\alpha_s(r)\hbar c}{r} + kr \tag{2.1}$$

Here α_s is the coupling constant of the strong interaction, r is the distance between quark and antiquark and k is a coefficient for the linear term, which is called the *string tension*. At large distances the first part of this potential vanishes, while the second part is getting larger. The *string tension* is a result of the mentioned interactions between the gluons to themselves. If one is looking at an interaction between two quarks via a virtual gluon this virtual gluon can produce additional virtual gluons since they are massless. The bigger the distance gets the more virtual gluons get produced and at some point the energy of the gluon field gets high enough to produce a real quark-antiquark pair. This is called *string breaking*. Afterwards the force

$$\begin{aligned}
\psi_1 &= |r\bar{g}\rangle\,, & \psi_2 &= |r\bar{b}\rangle\,,\\
\psi_3 &= |g\bar{r}\rangle\,, & \psi_4 &= |g\bar{b}\rangle\,,\\
\psi_5 &= |b\bar{r}\rangle\,, & \psi_6 &= |b\bar{g}\rangle\,,\\
\psi_7 &= \frac{1}{\sqrt{2}}\left(|r\bar{r}\rangle - |g\bar{g}\rangle\right)\,, & \psi_8 &= \frac{1}{\sqrt{6}}\left(|r\bar{r}\rangle + |g\bar{g}\rangle - 2|b\bar{b}\rangle\right)\,.
\end{aligned}$$

Figure 2.3: Gluon wave functions of the 8 colour states. [Picb]

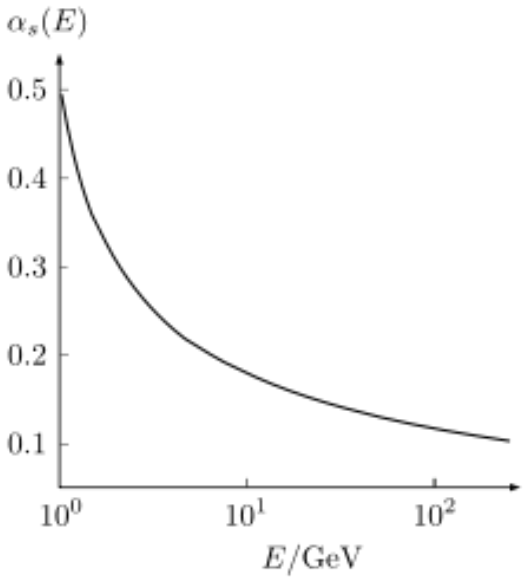

Figure 2.4: Coupling constant of the strong interaction as a function of energy transfer [Picc].

will act between the original quarks and the newly produced ones.
Because of the confinement one normally can not observe any free quarks. Instead the strong interaction has to be studied via hadrons which are colourless since the colours add up to colour neutral. This is called *confinement*. However, at very small distances or at very large momentum transfers the coupling constant vanishes and the confinement is released (*deconfinement*) [Chr17].

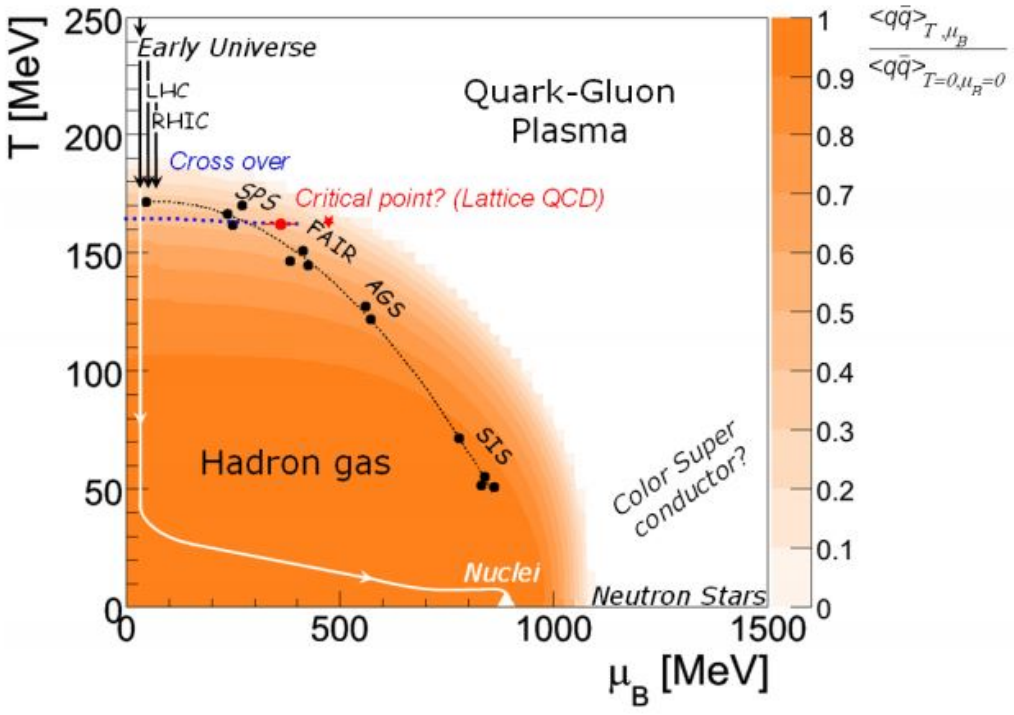

Figure 2.5: Phase diagram of strongly interacting matter with data points in the T and μ_B plane. The quark condensate ratio $\frac{<q\bar{q}>_{T,\mu_B}}{<q\bar{q}>_{T=0,\mu_B=0}}$ is the colour coded third dimension [Gal09].

2.3 The phase diagram of strongly interacting matter

The ***Q**uark **G**luon **P**lasma* (QGP) is a state of very high temperatures and/or net-baryon densities so that a state of deconfinement can be reached (Fig. 2.5). One expects that the hadron gas will cross over to a phase where the quarks will be quasi-free. Depending on the chemical potential μ_B it is expected to find different kinds of phase transitions. For small chemical potentials a smooth transition from a hadron gas to quark gluon plasma is expected. This is called *crossover*.

The region of special interest for the CBM experiment is the region of moderate temperatures and high net-baryon densities μ_B. Because of the so-called *sign problem* the lattice QCD calculations can not use standard Monte-Carlo methods and are not yet able to make firm predictions. But effective model calculations predict structures in the phase diagram like a critical endpoint followed by a first order phase transition. Also, there is the prediction of a

quarkyonic phase which has properties of high density baryonic matter and deconfined and chirally symmetric quark matter [T. 16a].

Chiral symmetry is one of the symmetries of the QCD Lagrangian and is exactly realized if quarks have zero mass. It is found to be spontaneously broken in nature. Because of their very small masses, the up and down quark can be considered as approximately chirally symmetric. The ground state of the QCD vacuum is populated by scalar quark-antiquark pairs ($< q\bar{q} >$ condensate). The interaction of such an $q\bar{q}$ pair with a left-handed quark q_L can convert it into a right-handed quark q_R. Due to the condensate, chiral symmetry is spontaneously broken and this condensate therefore acts as indicator for the chiral symmetry breaking. At very high baryon densities it is expected that the chiral condensate is reduced and the chiral symmetry is restored [Gal09].

2.4 Observables

It is not possible to pin down one single observable that satisfies all needs but instead physicists are looking for a variety of observables. A high production rate of hadrons containing strangeness and discrepancies of the J/ψ suppression are handled as promising signatures. In the end a combination of different observables can maybe give sufficient information about the system.

Since the purpose of the ***T****ransition* ***R****adiation* ***D****etector* (TRD) is the separation of electrons and pions, I will shortly speak about measurements of dileptons and about the J/ψ.

2.4.1 Dileptons

Dileptons are pairs of leptons and antileptons. Their special feature is that they do not interact via the strong interaction and therefore can leave a strongly coupled medium freely. Thus, they can transmit information about the different phases of the fireball and offer the opportunity to look into its temperature evolution and are expected to provide information about the lifetime of the fireball and the chiral symmetry restoration.

The most common dilepton pairs are e^+e^- pairs, since due to their low rest mass they can be generated into a large phase space. Depending on their invariant mass they are categorized into low-mass, intermediate-mass and high-mass regions.

In the range low-mass range the primary source of dileptons are light vector mesons like the ρ, ω and the ϕ. Discrepancies in this region between heavy-ion collisions and pp collisions, which can be observed as enhanced yields can be explained by hadronic in-medium interactions.

The intermediate mass range between the ϕ and the J/ψ is of special interest, since for center-of-mass energies below the point where charm production is getting dominant one has direct access to dileptons coming from thermal sources. Measurements like this enable studies of thermal properties of the early stages of the produced medium and this might also allow to look at the thermal radiation of the QGP phase. In [RvH16] and [Gal14] it is further explained that this energy range is of special interest, because of the possibility to map out the transition regime between partonic and hadronic matter. For instance, there might be a plateau in the energy dependence of the caloric curve, which would indicate a first order phase transition [wg16] [T. 16a].

In the high invariant mass range quark-antiquark annihilation of charm and anticharm or bottom and antibottom are the primary processes. The annihilation of these quark-antiquark pairs leads to the creation of a virtual photon which immediately decays into two leptons. The resulting lepton pair corresponds directly to the invariant mass of the quark-antiquark pair. The production probability and the momentum distribution correspond to those of the quark-antiquark pairs.

The CBM experiment will be able to have a look into the whole range of invariant masses with a sufficient statistical accuracy. One can expect several processes that will be contributing to the dilepton yield as shown in Fig. 2.6 [T. 16a]. The thermal radiation includes a broadened in-medium ρ meson, radiation from the QGP and dileptons from multi pion annihilation. Also the chiral mixing is reflected by the $\rho - a_1$ mixing which provides information about the chiral symmetry restoration. The main experimental challenges are the very low cross sections of the relevant processes and the combinatorial background. But since one primary goal of the CBM experiment in general is to investigate rare events, this challenges can be compensated by the large total amount of statistics collected [T. 16a].

As mentioned above one important task of the CBM experiment will be the measurement of dileptons in the intermediate mass range where quark-antiquark annihilation and charm decays are not yet dominant. A precise measurement of the spectral slope might allow for the determination of a

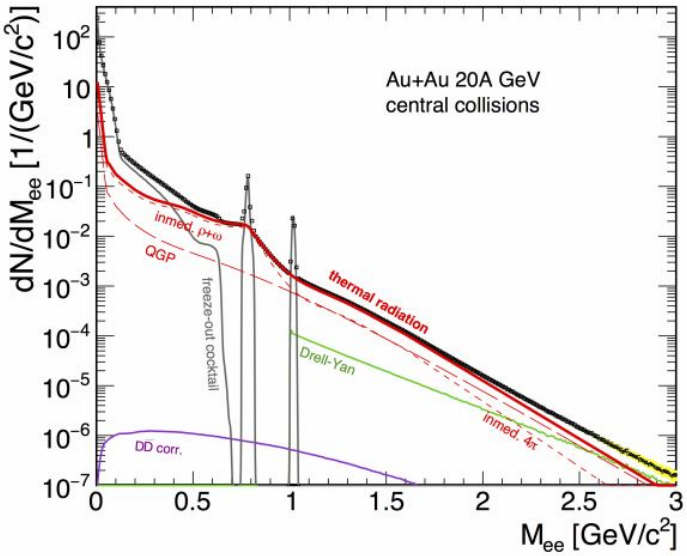

Figure 2.6: Invariant-mass spectrum of e^+e^- pairs radiated from a central Au+Au collision at 20A GeV beam energy. The solid red curve shows the contribution of the thermal radiation which includes in-medium ρ, ω spectral functions and QGP spectrum calculated using the many-body approach of [R. 99]. The freeze-out hadron cocktail (solid grey curve) is calculated using the Pluto event generator [I. 07] and includes two-body and Dalitz decays of π^0, η, ω and ϕ. Contributions of Drell-Yan (green solid curve) and correlated open charm (solid violet curve) have been simulated based on [ea14] [T. 16a].

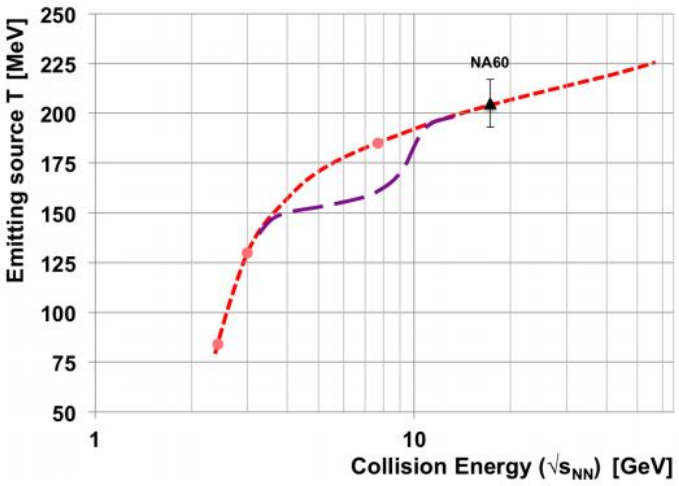

Figure 2.7: Excitation function of the fireball temperature T extracted from intermediate dilepton mass distributions as calculated with a coarse-graining approach (dotted red curve) [T. 16b]. The dashed violet curve corresponds to a speculative shape with phase transition occurring in the SIS100 energy range. The black triangle corresponds to the temperature as measured by the NA60 collaboration at SPS [H. 10]. [T. 16a]

caloric curve, which leads to a signature for a phase coexistence in highly dense nuclear matter. The excitation function of the fireball temperature extracted from the intermediate dilepton mass range, as calculated within a coarse-graining approach [T. 16b], is shown in Fig. 2.7 [T. 16a]. The red dashed line is showing the coarse gaining approach and the violet dashed line is showing a speculative curve in which the temperature saturates over a broad energy range. The observation of such a curve would clearly indicate a first order phase transition [T. 16a].

2.4.2 J/ψ

The J/ψ is a special observable in heavy-ion physics, since its production rate is supposed to change in a deconfined state of matter. Because of this it is a very promising observable for the investigation of the QGP. This so-called *J/ψ suppression* is the factor with which the production rate changes with different energies. It was already measured for high center of mass energies at SPS, RHIC and LHC, but the development in the direction of lower energies is not yet investigated. The TRD itself could deliver very important information to measure the J/ψ via its di-electron channel in this energy region [wg16].

The J/ψ consists out of a pair of charm and anticharm quark. The phenomenon of J/ψ suppression itself is explained by the fact that the charm-anticharm quarks will not be able to form a bound state when they are in the QGP phase. The charm and anticharm quarks are unable to bind because of the colour shielding of the other quarks and gluons in the medium. This is called *Debye-screening* which was first found in electromagnetic plasmas but also applies for the QGP [MS86].

Measurements with different p+A collisions at up to 30 GeV are supposed to investigate the charmonium interaction with cold nuclear matter and contribute a baseline for measurements in nuclear collisions. CBM at SIS100 will study charm production with energies near the production threshold, where the formation time is comparably small to the lifetime of the fireball. CBM will also use J/ψ as a probe of the hot medium to lower energies. Measurements of symmetric nuclei will be done with energies up to 15 A GeV and below threshold in Au+Au collisions at 10 A GeV [T. 16a].

3 The experiment

3.1 FAIR

The *Helmholtzzentrum für Schwerionenforschung* was founded in 1969 and the first beam was delivered by the *UNILAC* in 1975. Already in the 1980ties the GSI was able to synthesise multiple super heavy elements. Later the synchrotron SIS18 was added, as well as the heavy-ion storage ring ESR [Wen08]. The newest extension is the ***F****acility for* ***A****ntiproton and* ***I****on* ***R****esearch* (FAIR) which is currently being planned, prepared and build and should be operational in 2023. Figure 3.1 shows an overview of the planned experiment area.

Initially the extension was planned with two new synchrotrons. These are the SIS100 and the SIS300 named after their electromagnetic rigidity of 100 Tm and 300 Tm. The rigidity is a crucial parameter for the achievable energies of the particles. Currently the plans are reduced to the construction of the SIS100 which will lead to lower collision energies but should still offer a promising physics case due to high beam intensities. An important parameter will be the luminosity.
The luminosity can be defined as the product of the number of arriving ions per time $\frac{dN_i}{dt}$, the density of the target ρ_T and the targets thickness l:

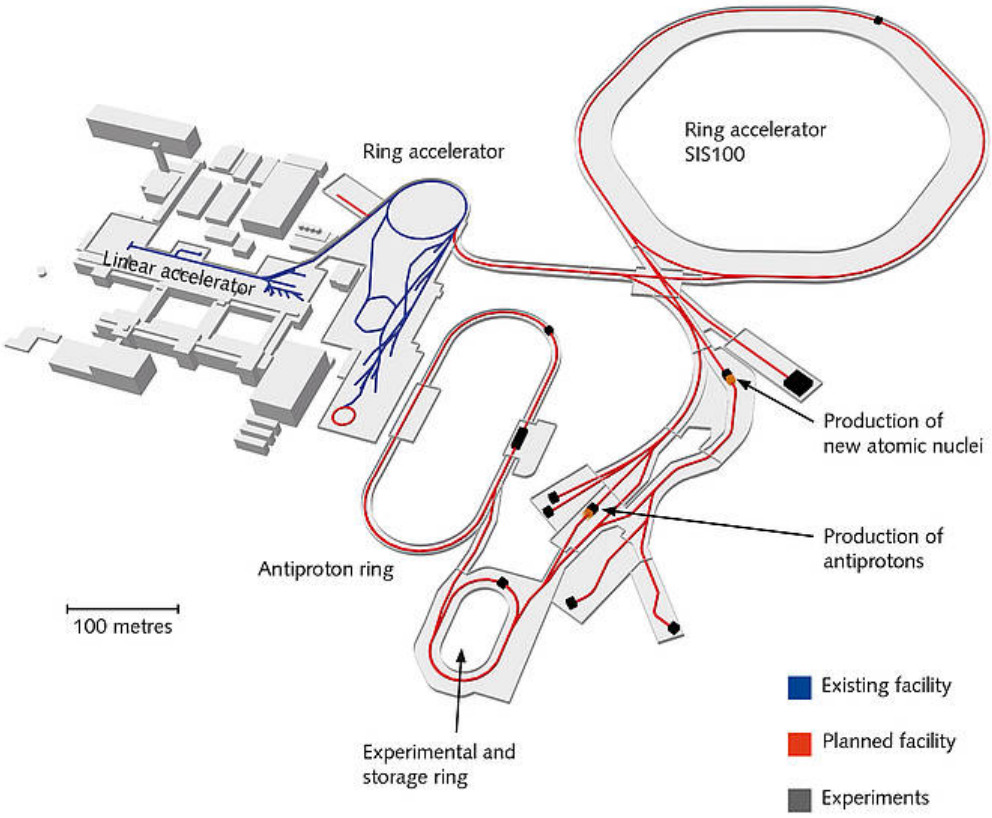

Figure 3.1: Overview of the planned accelerator area at FAIR together with the existing facilities of the GSI. [Fai].

$$L = \frac{dN_i}{dt} \cdot \rho_T \cdot l \tag{3.1}$$

The product of the luminosity and the cross section then leads to the expected interaction rates:

$$R = L \cdot \sigma \tag{3.2}$$

Interaction rates of up to 10 MHz are foresee, which is an outstanding value and will allow CBM to perform high statistics measurements [T. 16a].

Besides the CBM experiment there are three other big projects that are going to be build. There is the *Anti**P**roton **AN**ihilation at **DA**rmstadt* (PANDA), the ***A**tomic,**P**lasma **P**hysics and **A**pplications* (APPA) and the ***NU**clear **S**tructure, **A**strophysics and **R**eactions* (NUSTAR) project.
The APPA group will be studying the behaviour of plasmas at high pressures but low temperatures and they also want to investigate the impact of cosmic radiation on inter-planetary flights for astronauts and spacecraft components [APP].

The NUSTAR collaboration will try to achieve a better understanding of heavy and exotic matter, because it is assumed that chemical elements heavier than iron originate from collapsing stars or stellar collisions. They also try to investigate the nuclear forces and the symmetries in rare isotopes. This should give a deeper insight into the interior of neutron stars and other astrophysical questions [NUS].

The PANDA experiment is going to investigate the strong interaction with special regard to the generation of mass. Since just a small fraction of the hadron mass is equal to the actual rest masses of the quarks, the rest of the mass has to be generated in a different way. They will use proton-antiproton annihilation reactions which produce a large amount of gluons and maximizes the chances to study the interaction between gluons in the so called *glueballs* which is done with hadron spectroscopy [PAN].

3.2 The CBM experiment

The CBM experiment will be able to investigate strongly interacting matter at high densities through rare probes. For this purpose a large event statistics is required. This means that a very fast detector design is needed together

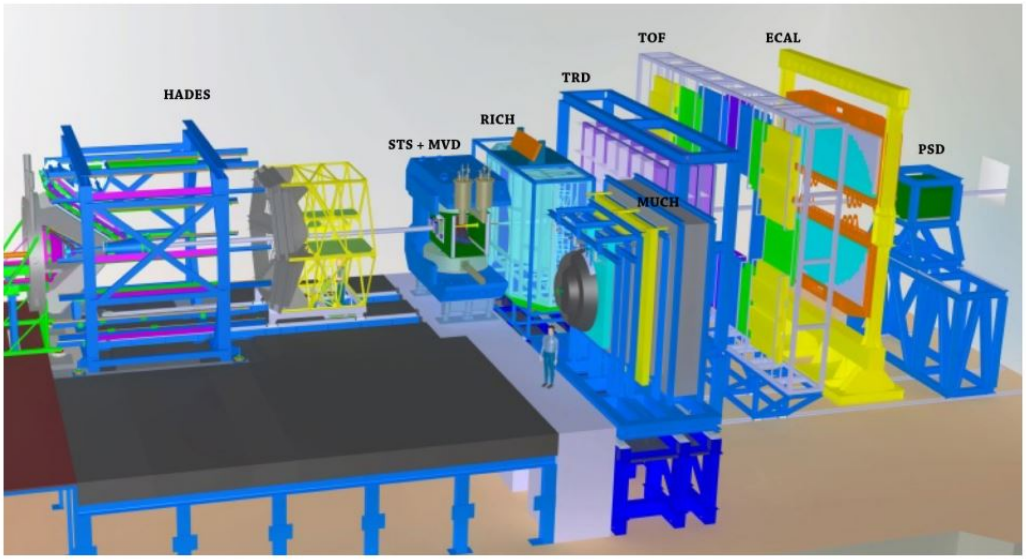

Figure 3.2: Overview of the CBM setup with the HADES detector on the left hand side. The electron and muon setup is getting realised by the exchange of RICH and MUCH [T. 16a].

with fast electronics so that the high interaction rates can be handled.
The experiment is suited to measure at the full FAIR beam energy range and is designed to measure hadrons, electrons and muons.

A field of particular interest will be the measurement of light vector mesons like the ω, ρ and ϕ. These decay into mesons and dileptons. Especially the dilepton channels offer a lot of information about the system since the leptons do not interact via the strong interaction and are thus not disturbed by the hadronic medium. On the other hand the dileptons interact via the electromagnetic interaction and therefore their production rate is proportional to the much lower electromagnetic coupling constant of ($\alpha^2 = \frac{1}{137^2}$). For this reason there is again the need for high interaction rates to gather sufficient statistics.

The modular design of the CBM experiment, will allow two separate measurement setups. These two setups will be specialised in measuring electrons and muons, respectively. This approach allows to gather two systematically different but comparable sets of data. The setups can be switched by the replacement of RICH and MUCH (see Fig. 3.2). The sub-detector that is not used can be placed in a parking position [BF09].

In both cases, the first two sub-detector systems will be the ***M**icro **V**ertex **D**etector* (MVD) and the ***S**ilicon **T**racking **S**ystem* (STS). The MVD is designed to make very high resolution measurements of the secondary vertex position and the STS is essential for the track reconstruction. They are going to be placed inside a superconducting magnet.
The next sub-detector system differs depending on the setup. For the electron setup it is the ***R**ing **I**maging **C**herenkov **D**etector* (RICH), which can identify electrons up to a momentum of 6-8 GeV/c.
In case of the muon setup the next sub-detector after the STS is the ***M**uon **T**racking **CH**amber* (MUCH). The MUCH is basically a lot of material to absorb everything besides the wanted muons. This is done via multiple iron layers. Additionally there is a tracking system for the muons.
Afterwards there is the ***T**ransition **R**adiation **D**etector* (TRD) ,which can identify electrons up to a very high momentum. It is supposed to expand the identification capabilities of the RICH for momenta above 6 GeV/c. The region where the identification of TRD and RICH overlap is also getting significantly improved by the combination of both sub-detectors.
The ***T**ime **O**f **F**light* (TOF) detector is the following sub-detector system. It consists out of ***R**esistive **P**late **C**hambers* (RPC) and is able to identify charged hadrons via their correlation between their mass and the time they need to pass the sub-detector.
The last stations are the ***E**lectromagnetic **CAL**orimeter* (ECAL) for the electron setup and a ***P**rojectile **S**pectator **D**etector* (PSD) which is going to measure collision centralities for both setups [BF09].

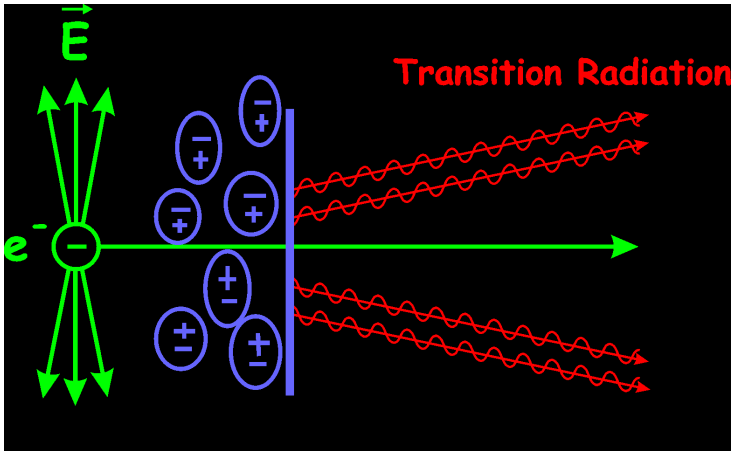

Figure 3.3: Schematic view of transition radiation production at a single boundary. The electron is propagating to the boundary and creates an electric field which will vanish and create a photon [TR].

3.3 The transition radiation detector

The basis of a TRD is the ***T****ransition* ***R****adiation* (TR) which is also responsible for the name of the detector. TR production is a statistical process that occurs when a charged particle crosses the boundary between two media with different dielectric constants ϵ. The TRD as a whole consists out of the *radiator* and the *read-out detector*. A careful selection of all the used materials and configuration parameters is needed to optimize this detector, especially in case of the CBM where a very fast detector is needed.

3.3.1 Transition radiation

A simple way to describe this phenomenon is the usage of a mirror charge which gets induced inside the second medium by the charged particle flying through the first medium. These two charges create an electric dipole field that stores a certain energy. While the charged particle is moving in direction of the boundary, the electric field changes and in the end vanishes at the boundary. The previously stored energy then gets emitted via a photon (Fig. 3.3).

An important fact about the transition radiation is that it depends on the Lorentz factor γ of the charged particle. This means that the probability for transition radiation production drastically differs for different masses of the particles, since low mass particles reach a much higher value of γ than

heavy particles. The electron is a very low mass particle and therefore has a much higher probability to produce transition radiation than for example a pion. That is the reason why the TRD is assigned with the task to separate electron and pions.

For highly relativistic particles with $\gamma \gg 1$ the dielectric constant of the medium is given by:

$$\epsilon^2 = \frac{\omega_P^2}{\omega^2} \tag{3.3}$$

Where ω_P^2 is the plasma frequency of the medium and ω is the frequency of the emitted photon. The plasma frequency is calculated as:

$$\omega_P = \sqrt{\frac{4\pi\alpha n_e}{m_e}} \approx 28.8\sqrt{\rho\frac{Z}{A}}\text{eV} \tag{3.4}$$

Where n_e is the density of the electrons and m_e is their mass. With these formulas one can calculate the differential energy spectrum and the intensity:

$$\frac{d^2W}{d\omega d\Omega} = \frac{\alpha}{\pi^2}\left(\frac{\Theta}{\gamma^{-2}+\Theta^2+\epsilon_1^2} - \frac{\Theta}{\gamma^{-2}+\Theta^2+\epsilon_2^2}\right)^2 \tag{3.5}$$

$$S_0 = \int\int\left(\frac{d^2S_0}{d\Theta d\omega}\right)d\Theta d\omega = \frac{\alpha\hbar}{3}\frac{(\omega_{P_1}-\omega_{P_2})^2}{\omega_{P_1}+\omega_{P_2}}\gamma \tag{3.6}$$

Here is Ω the emission angle of the emitted photon relative to the trajectory of the charged particle and α is the fine structure constant.
One can clearly see that the emitted photons will most probably be emitted at small emission angles Ω. Also one observes a linear dependence on the Lorentz factor and the so-called *cutoff frequency* around $\omega = \omega_1 \cdot \gamma$. Due to the low probabilities for transition radiation in general the photon yield is very low (Fig. 3.4). The TR production can be increased by introducing a large amount of boundaries. This can be achieved with *regular* or *irregular* radiators [AW12] [CHMP74].

3.3.2 The radiator

For ID purposes one has to optimize the energy spectrum and intensity of TR production. As already mentioned there are two general types of radiators.
The regular radiator consists of several layers of a foil with clearly defined distances between each foil. The advantage of this approach is that such a radiator is comparably easy to calculate and simulate as one can see in the

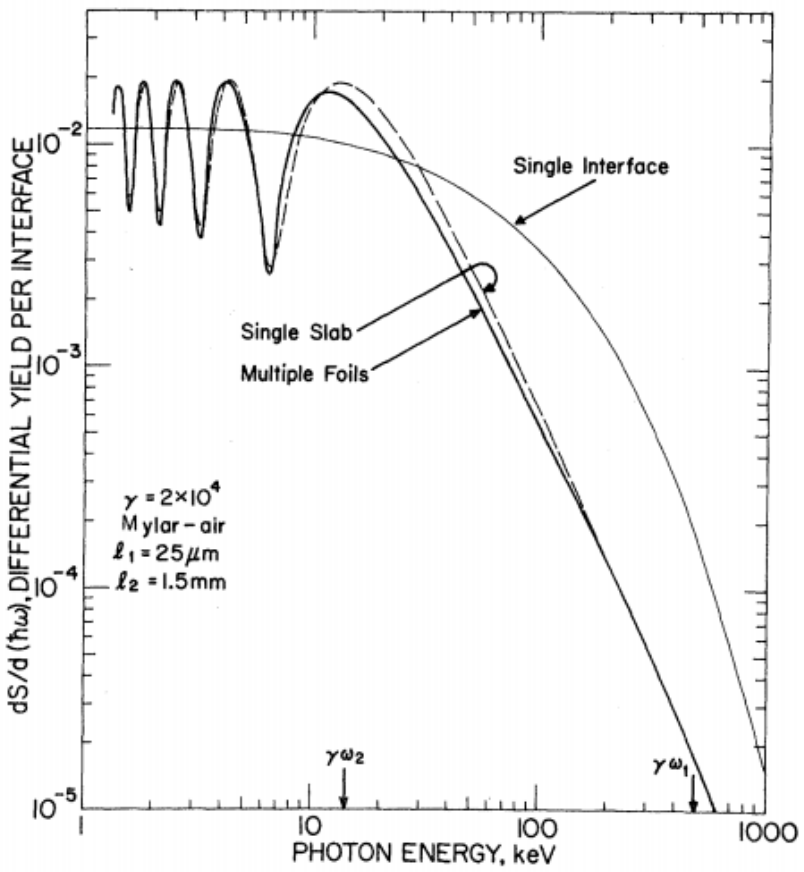

Figure 3.4: Photon yield depending on the photon energy for a single transition and for multiple foils [AW12].

following equation [wg16]:

$$\frac{dN}{d\omega} = \frac{4\alpha}{\omega(\kappa+1)} \frac{(1-\exp^{(-N_f\sigma)})}{(1-\exp^{(-\sigma)})} \cdot \sum_n \Theta_n \left(\frac{1}{\zeta_1+\Theta_n} - \frac{1}{\zeta_2+\Theta_n} \right)^2 [1-\cos(\zeta_1+\Theta_n)] \tag{3.7}$$

$$\kappa = \frac{l_2}{l_1} \tag{3.8}$$

$$\Theta_n = \frac{2\pi n - (\zeta_1 + \kappa\zeta_2)}{(1+\kappa)} > 0 \tag{3.9}$$

$$\zeta_i = \frac{\omega l_1}{2c} \left(\gamma^{-2} + \left(\frac{\omega_{P,i}}{\omega} \right)^2 \right) \tag{3.10}$$

Here is N_f the number of foils, l_1 is the thickness of the foils, l_2 is the distance between the foils and $l_1 < l_2$.

Figure 3.5 shows the yield of transition radiation photons as a function of their energy depending on the Lorentz factor, the thickness of the foils and the distance between two foils. As one would expect the yield of TR photons increases with the Lorentz factor while the shape of the energy spectrum does not change (first panel of Fig. 3.5). The same effect occurs when one varies the distance between two foils as one can see in the third panel of Fig. 3.5. A larger distance between the foils creates a higher yield but does not influence the spectrum. The variation of the thickness of the foils on the other hand changes the shape of the spectrum (second panel of Fig. 3.5). The maximum of the yield moves to higher energies with increasing thickness of the foils.
The advantages of a regular radiator a very clear. A regular radiator offers the possibility to calculate the expected outcome and simulate and compare different materials. The only problem with this approach is the fact that it is comparably difficult and expensive to build a regular radiator.

The alternative are irregular radiators. This type of radiators are mostly build out of foams and fibers. The distances between two boundaries is not uniform and it is not possible to calculate the outcome for the transition radiation directly. However, the parameters for every boundary are statistically distributed and on the average the variances should compensate.
The big advantage of irregular radiators is the fact that they are comparably cheap and easy to produce. The characteristics of the specific irregular radiator are tested experimentally and one has to check different materials until one finds the material with the right characteristics for the experiment. For

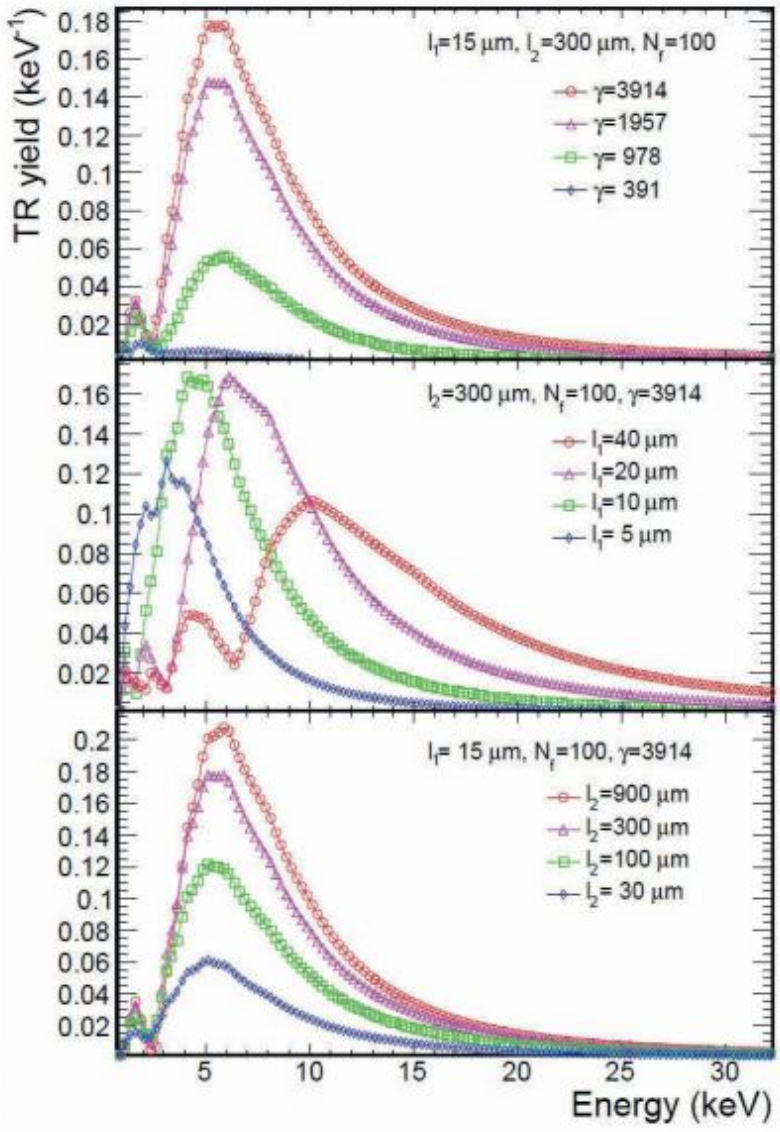

Figure 3.5: Yield of transition radiation photons depending on their energy [And11]. The three panels show different variations of the parameters l_1, l_2 and γ.

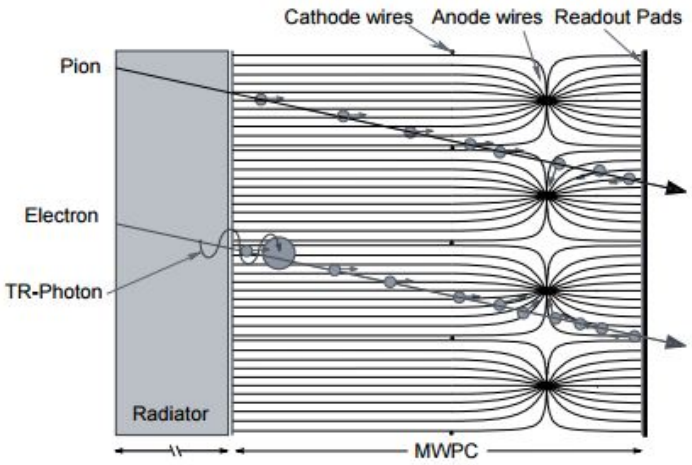

Figure 3.6: Schematic overview of a MWPC [Are14]

simulations the irregular radiators often get approximated by regular radiators with comparable characteristics. The CBM experiment will use irregular radiators.

3.3.3 Multi-Wire Proportional Chamber

A ***M**ulti-**W**ire **P**roportional **C**hamber* (MWPC) primarily consists of a set of thin parallel and equally spaced anode wires in between two cathode planes (Fig. 3.6). One reason why MWPCs are interesting for experiments like the CBM is the fact that they are relatively affordable to build for large detectors and that particles can pass them without being influenced too much.

The actual read-out detector is placed right behind the radiator and it is designed to measure the energy deposition of charged particles and the transition radiation photons passing through.

The cathode planes are on ground potential while the anode wires are supplied with a positive potential. The potential is chosen such that the multiplication is in the region of proportionality (Fig. 3.7). After a particle passes the entrance window (the first cathode plane) it is able to ionize the gas inside the chamber which creates electron-ion pairs inside the chamber. The electric field between the cathode planes and the anode wires accelerates the electrons from the ionization in the direction of the anode wires. The accelerated electrons then also ionize gas particles in a so called *secondary*

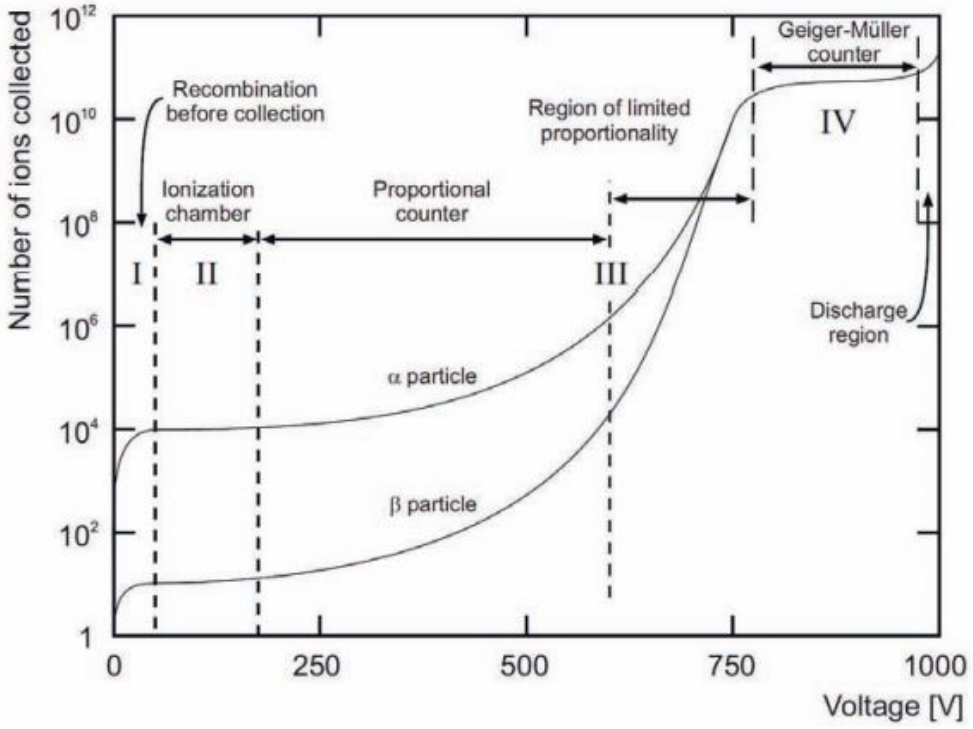

Figure 3.7: Ion yield versus the potential on the anode wires [Cyr09]

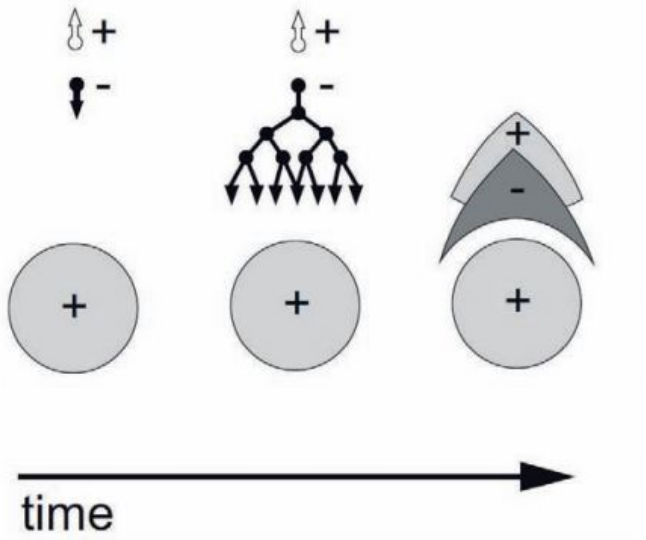

Figure 3.8: Avalanche of electrons in a MWPC [Cyr09]

ionization. This secondary ionization gets very high near the anode wires since the electrons feel the electric field strongly in this region. Avalanches of electrons occur and their characteristics depend on the chosen gas in the chamber (Fig. 3.8).
The multiplication of ionization electrons is called *gas amplification* or *gas gain* and it depends on the potential of the anode wires. With this information one is able to reconstruct the total energy deposition inside the chamber. What one measures in the end is the charge induced by the ions drifting slowly inside the chamber. To obtain two dimensional information of the position of the charged particle passing through the detector the exit plane gets divided into several electrodes called *pads*. The signal is induced on several pads and collected by these pads.

Gas amplification
Another important aspect of the read-out detector is the selection of the right gas mixture inside the chamber, since the gas mixture is responsible for the necessary gas amplification. The gas should also be able to absorb the TR photons that are produced in the radiator and emit electrons through ionization. The cross section for these interactions increases with the atomic number. Therefore Xenon (Xe) is a good candidate, since it is the heaviest non-radioactive gas. Xenon uses the main fraction of the energy for ionization.

Also, not all ionized gas atoms directly return to their ground state. In some cases they return to their ground state via an intermediate stage with the emission of an additional photon. In this situation the extra photon is able to create a contribution to the signal which does not correspond to the actual energy deposition of the initial energy deposition. This effect decreases the precision of the measurement and therefore there has to be a so-called *quenching gas* added to the gas mixture. This quenching gas is supposed to absorb such photons. A commonly used quenching gas is CO_2.

The actual gas amplification is correlated to the electric field, the first Townsend coefficient, which expresses the number of ion pairs generated per unit length, the excitation and ionization cross section of electrons and the density of the ionizing gas. The Townsend coefficient has to be measured, since it can not be calculated analytically. The increase of electrons in comparison to the number of electrons before the amplification N_0 is defined by:

$$G = \frac{N(s_a)}{N_0} = \exp\left(\int_{s_0}^{s_a} \alpha(E(s))ds\right) \tag{3.11}$$

This goes over into the so-called *Diethorn-Formula* with a few steps. The formula delivers a good approximation for a lot of detector geometries. For a cylindrical geometry the gain factor becomes:

$$G = \exp\left(\frac{U}{\ln(\frac{a}{b})}\int_{E_{min}}^{E_a} \frac{\alpha(E)}{E^2}dE\right) \tag{3.12}$$

Where E_{min} is the minimal electric field to generate multiple ionizations, a is the wire radius and b is the length of the drift chamber.
The approximation uses the assumption that $\alpha(E) = kE$. With this one gets:

$$\ln(G) = \frac{kU}{\ln\frac{a}{b}} \cdot \left(\frac{E(a)}{E_{min}}\right) \tag{3.13}$$

To calculate the value of k one uses the expected number of ionizations via $m = \frac{\Delta\phi}{\Delta U}$. Here is ΔU the potential that is needed to accelerate an electron to the ionization energy of the gas and $\Delta\phi$ is the total potential difference in the amplification region:

$$\Delta\phi = \int_0^{r(E_{min})} E(r)dr = \frac{U}{\ln\cdot\frac{b}{a}} \ln\left(\frac{E(a)}{E_{min}}\right) \tag{3.14}$$

With the assumption that the number of electrons doubles with every interaction ($G = 2^m$) one gets:

$$\ln(G) = m \cdot ln(2) = \frac{U \cdot \ln(2)}{\ln(\frac{b}{a})\Delta U} \ln\left(\frac{E(a)}{E_{min}}\right) \tag{3.15}$$

and by comparison to formula 3.13: $k = \frac{\ln(2)}{\Delta U}$
Together with the replacement of $E(a)$ for a given voltage this leads to the Diethorn-formula [Blu16]:

$$E(a) = \frac{U}{a \cdot \ln(\frac{a}{b})} \tag{3.16}$$

$$E_{min}(p) = E_{min}(p_0)\frac{p}{p_0} \tag{3.17}$$

$$\ln(G) = \frac{U \cdot \ln(2)}{\ln(\frac{a}{b})\Delta U} \cdot \ln\left(\frac{U}{a \cdot \ln(\frac{b}{a}E_{min}(p_0)\frac{p}{p_0})}\right) \tag{3.18}$$

4 Analysis

The next chapter are about the development of a well functioning likelihood method for particle identification. This includes the implementation of the method, the investigation of *V0-Topologies* as candidates for later data taking needs, studies of expected production rates and possible statistics and performance studies for the TRD with the usage of the likelihood method as well as the investigation of di-electron channels.

There are two primary methods for particle identification with the TRD. One is the likelihood method and the other one is the artificial neural network. Until now the primarily used method for particle identification with the TRD was the ***A****rtificial* ***N****eural* ***N****etwork* (ANN) which delivered good results. The reason for the implementation of an alternative method is the fact that the ANN is very hard to diagnose in case of performance problems. Since the network has to be adjusted in a very sensitive balance of all the weights and thresholds on the neurons, it is not possible to correct or even identify misbehaviours by hand.
Another aspect of this consideration is the fact that it is only possible to train the network with MC-simulation data and therefore it is also possible that in the later data taking one gets slightly different measurements in comparison to the simulations which then could lead to a strong effect on the identification performance. This possible effect again corresponds to the nature of the network which is by definition dependent on a very precise training. Also the strength of the ANN lies in the analysis of several variables at once, but the TRD only measures one input value, which is the energy deposition.

The likelihood method on the other hand is very intuitive and can be easily understood in its behaviour. The final likelihood values and the uncertainties for particle misidentification can be investigated for the measured energy deposition or the number of hits in the different TRD layers. In principle, the likelihood method does also depend on training data, because of the necessary probability distributions, but these are much easier to understand and analyse in case of identification misbehaviour.

The performance of both methods seems to be comparable for the possible simulation studies by now as it will be further discussed in the following sections.

4.1 Simulation

The basis of the simulation as well as all the analysis is the CBMROOT framework which is written in C++. CBMROOT supports several external particle generators like *UrQMD* and *PLUTO* and transport algorithms which create the detector responses. Here used is *GEANT3*, hwich includes the geometries of the CBM detector system including all the sub-detectors as well as the beam pipe and the magnet [wg16].

The MVD which is equipped with high resolution sensors (22x 33 μm^2 pitch) and realistic material budget and in the position of the dilepton configuration (z = 80, 120, 160 and 200 mm), where z is the distance to the target. The MVD delivers a good resolution on the secondary vertex.

The STS consists of eight tracking stations consisting out of double sided silicon strips with a thickness of 300 μm and a pitch of 58 μm. The tracking stations are positioned at equal distances between 30 cm and 100 cm away from the target.

For the RICH detector a mirror with a tilt of 10° is taken into account. Together with photon sensors and a large amount of read-out channels, the RICH detector is able to separate electrons and pion up to a momentum region of 8 GeV/c. It is mounted on a carbon structure combined with a grid of aluminium tubes. The multi anode photomultipliers are shielded by two steel boxes, so that they do not get in contact with the magnetic stray field.

The TRD consists out of four detector layers. It is composed of the radiator and the ***R**ead-**O**ut **C**hamber* (ROC). The ROCs are designed as multi-wire proportional chambers with an amplification region of 3.5+3.5 mm thickness and a drift region of 5 mm. Their implementation in the simulation framework can be seen in Fig. 4.1.

Lastly, the TOF is positioned at a distance of 10 m to the target. The simulation includes the full simulation chain with digitization and clustering [wg16].

The simulation itself is done in three major steps. First events are generated via *UrQMD* and *PLUTO*, followed by the simulation step, which includes the transport through the detector which is done with *GEANT3*. In the end the reconstruction is done, which also includes the TRD response

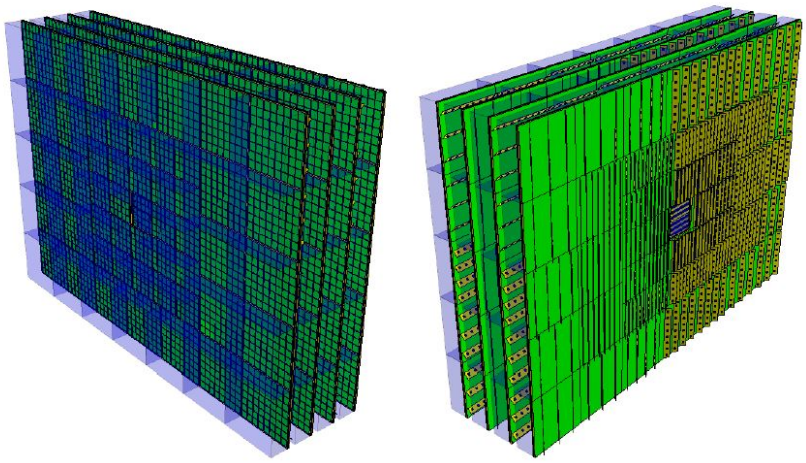

Figure 4.1: CBM-TRD geometry for SIS100, consisting of one station with four layers of detectors. On the left side is the front view on the radiator boxes and on the right side is the view on the backpanels with the front-end electronics. [wg16]

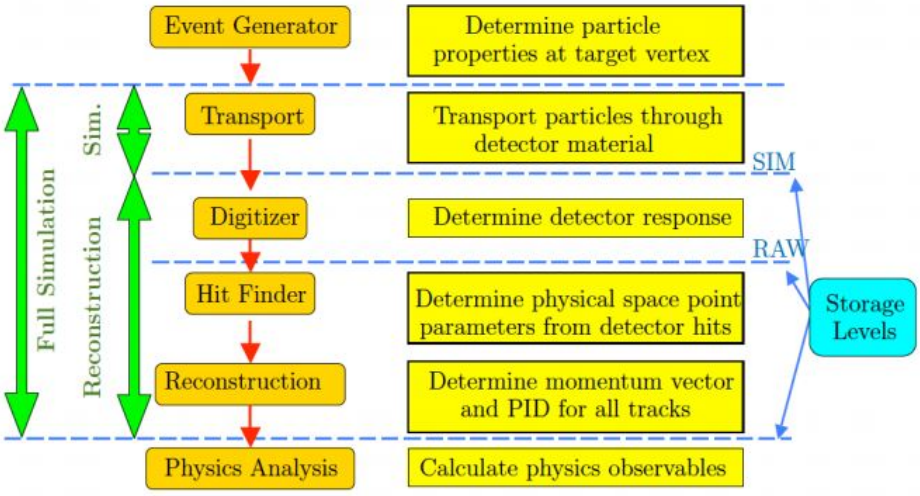

Figure 4.2: Overview over the different steps in the simulation process [T. 16a]

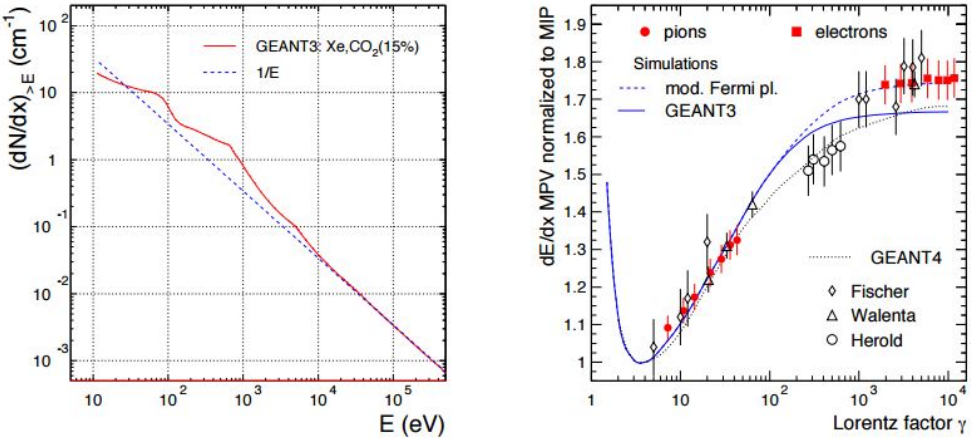

Figure 4.3: Left: Comparison of the integral spectrum of energy transfer results for GEANT3 and a Rutherford spectrum. Right: Comparison of the most probable energy loss values for simulation and data normalized to the MIP value. [ea04]

simulation and the signal generation (Fig. 4.2) [wg16].

The energy loss is simulated with *GEANT3*. *GEANT3* uses an implementation of the photo-absorption ionization model [All80] for the calculation. In Figure 4.3 one can see a comparison of a Rutherford spectrum and the results of *GEANT3* for the energy spectrum of primary electrons released in inelastic collisions of minimum ionizing particles. The corresponding gas is a mixture of Xe and CO_2. The comparison starts at the energy value of 12.1 eV as this is the ionization potential of Xenon and extends to the region where the electrons are treated as δ-rays, for which the threshold has been chosen to be 10 keV. One can also see on the right side of Fig. 4.3 a comparison of the most probable energy loss values between simulation and data [wg16].

The simulation of **T**ransition **R**adiation (TR) takes into account the absorption in the radiator, in the aluminized entrance window and the entrance foil, in the lattice grid and in the gas. The photon spectrum for the integrated emission angle θ (emission angle relative to the direction of motion) can be approximated as a regular radiator by the equations 3.7-3.10 of Chap. 3.3.2.

The input for the simulation was calculated with *UrQMD* and corresponds to 10% most central Au+Au 8 A GeV events. The simulation for the following analysis is based on 5 million UrQMD events as hadronic background

Source	$BR_{e^+e^-}$	Total multiplicities	
		p + Au	Au + Au
ρ^0	$4.72 \cdot 10^{-5}$	$3.4 \cdot 10^{-3}$	9.0
ω	$7.28 \cdot 10^{-4}$	$5.7 \cdot 10^{-3}$	19.0
ϕ	$2.97 \cdot 10^{-4}$	$1.7 \cdot 10^{-4}$	0.12
J/ψ(1S)	$5.97 \cdot 10^{-2}$	$5.1 \cdot 10^{-8}$	—
ψ(2S)	$7.89 \cdot 10^{-3}$	$1.3 \cdot 10^{-9}$	—
In-medium radiation	—	—	$2.2 \cdot 10^{-2}$
QGP radiation	—	—	$5.8 \cdot 10^{-3}$

Table 1: Branching ratios and multiplicities of the dilepton signals in the simulation generated with PLUTO and based on the calculations of [F.] [T. 16b] [W.]

and additional dilepton signals generated with PLUTO and calculated with a many body approach (see Fig. 2.6) [R. 99] [F.]. The latter are created with the branching ratios and multiplicities as listed in Tab. 1. The CBMRoot version is the release of June 2016 and the used geometry is the standard geometry of the SIS100 electron setup with a target thickness of 25 μm.

4.2 Likelihood method and Artifical Neural Network (ANN)

Each set of data is normally characterized by a corresponding probability distribution which again is determined by the parameters that influence it. In the most simple cases one has got just one parameter that describes the distribution. The TRD is measuring the energy deposition of different particles which can then be used for particle identification.
In high energy physics one often has the reversed case where one has the data of the measurements and tries to investigate which probability distribution lies underneath. The power of the likelihood method is its potential to compare models and conclude which model is more likely to produce the given data.

The formula for a specific likelihood function is given by:

$$L(\Phi, x_1, ..., x_n) = f(x_1, x_2, ..., x_n|\Phi) = \prod_{i=1}^{n} f(x_i|\Phi) \tag{4.1}$$

Where x_i are the observed values and Φ is the functions parameter, which is

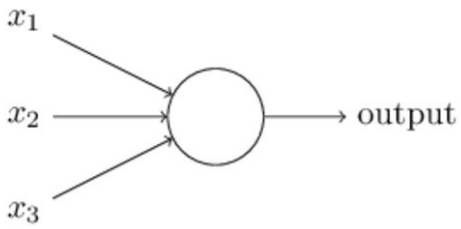

Figure 4.4: A perceptron with three input variables creating one output

allowed to vary freely.

The next step in the comparison of two models is to use the produced likelihood functions for a *likelihood ratio test*, which is a simple realisation of an hypothesis test with:

- H_0: $\mathbf{x}$ corresponds to likelihood function L_0
- H_1: $\mathbf{x}$ corresponds to likelihood function L_1

This results in a likelihood-ratio-value (LRV):

$$LRV = \frac{L_0}{L_1} \tag{4.2}$$

The LRV lies between 0 and 1 and has an uncertainty (ξ) of:

$$\xi^2 = -2 \cdot \ln\left(\frac{L_0}{L_1}\right) \tag{4.3}$$

This uncertainty will drastically increase with smaller LRV. In the case of high energy physics and more precisely for particle identification one can use this method to calculate a measured tracks probability to be of a certain particle type.

The common alternative to this method is the so called ***A**rtificial **N**eural **N**etwork* (ANN). It is widely used because of its very promising basic idea of a flexible and learning decision process. An artificial neural network goes into the direction of computer intelligence and machine learning by using a network of neurons which all produce little decisions.
To understand the way this works one first has to get an impression of what neurons do. The so-called *perceptrons* are the basic realisation of a neuron (Fig. 4.4). A perceptron takes a specific number of input variables and uses

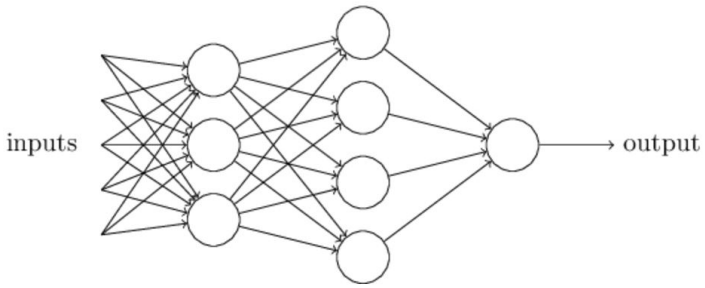

Figure 4.5: Neural network with perceptrons [Mic16]

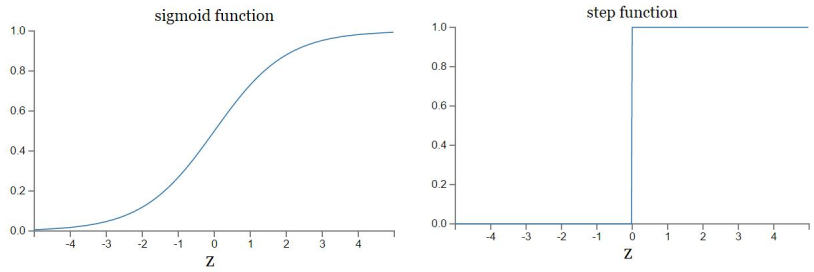

Figure 4.6: Left: Sigmoid function. Right: Step function [Mic16]

them to make a binary decision (0 for no and 1 for yes). Also the importance of different input variables can be modified through weights on each variable and the threshold can be varied. With careful variation of these parameters a very selective decision making can be achieved, even though the corresponding formula is pretty simple (Eq. 4.4) [Mic16].

$$\text{output} = \begin{cases} 0 & \sum_j w_j x_j \leq \text{ threshold} \\ 1 & \sum_j w_j x_j > \text{ threshold} \end{cases} \tag{4.4}$$

The potential of such neurons lies in the fact that they can be ordered to create an interconnected processing of the incoming information, so that they use a wide field of variables with different evaluations by the different neurons (Fig. 4.5).They are also capable of building logical functions (*and,or,nand*).
This kind of network would not yet be able to learn the right mix of weights and thresholds by itself. In fact, it would even be possible to destroy the whole decision making by very small variations, because of the binary character of the input and the output. Instead, one needs a network that creates minor variations in the output if it gets confronted with minor variations

in the input. A realisation of this requirement is possible with the usage of a continuous scale of values for input, weight and output instead of the binary one (this is then called a *sigmoid neuron* and a *sigmoid function*), which basically just replaces the step function by a smoother version (Fig. 4.6) [Mic16]:

$$\text{output} = \frac{1}{1 + \exp(-\sum_j w_j x_j - b)} \tag{4.5}$$

Here b is the equivalent of the previous threshold which, however, is influenced by the smoother character of the shape. With these modifications one has a network that is able to learn and can be trained. By varying the weights on each neuron, depending on how close the produced output is to the expected value, the network can be iteratively optimized [Mic16].

For the CBM-TRD a set of variables λ_i is used and given to the input neurons, since the direct usage of the measured energy loss did not lead to a robust training of the network [AAI+07]. The variables λ_i are described by:

$$\lambda_i = \frac{E_i - E_{mp}}{\xi} - 0.225 \tag{4.6}$$

Where E_i is the energy loss in the ith layer of the TRD and E_{mp} is the most probable energy loss. ξ corresponds to $\frac{1}{4.02} FWHM$ of the distribution.This alternative input parameter describes a separate weighting of the measured energy deposition in comparison to the most probable energy deposition and is designed to make the training more robust [wg16].

4.3 Energy deposition in the TRD and tests of the likelihood method

This mathematical approach of the likelihood method can be simplified and adjusted for the CBM-TRD. It is supposed to be used for particle identification or more specific for electron-pion separation.

The separation is done through the specific energy deposition of the electrons and pions. This is possible because the electrons produce transition radiation as discussed in Chap. 3.3.1 and as one can see in Fig. 4.7. The transition radiation photons create an additional contribution to the energy deposition which is measured in the TRD and produces higher energy depositions. This results in a widening of the energy deposition spectrum of the electrons in comparison to π. The maximum value is still in the region of low energy depositions but the probability for energy depositions larger than 10

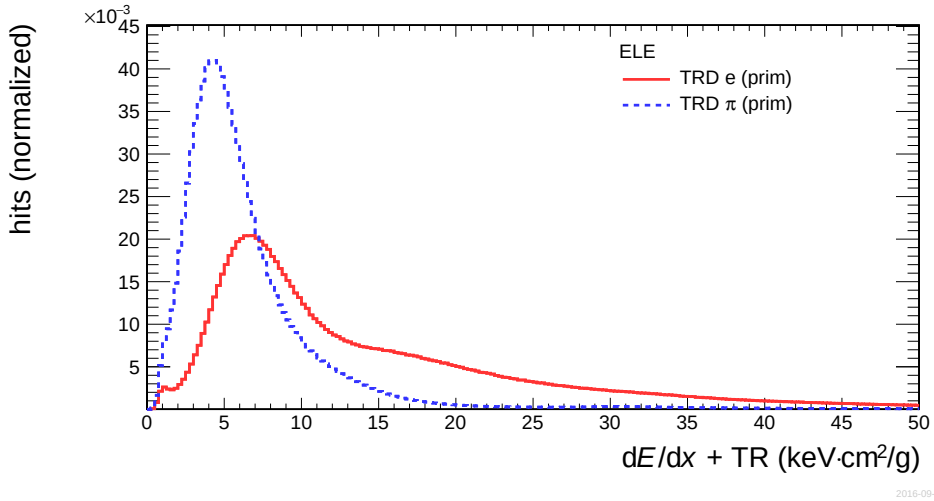

Figure 4.7: Normalized energy deposition spectrum for pions and electrons including all momenta. Particle identification was made via matching the reconstructed tracks to their MC tracks. The electron spectrum is showing a wider spectrum with higher energy depositions resulting from the TR photon contribution.

keV is drastically increased. The probability for pions to create such energy deposition values also never is zero, but the difference is in several orders of magnitude.
The likelihood ratio method uses differences in the probabilities to determine how well an observation can be explained through a specific model (Eq. 4.2). In our case of only two probability distributions the equation reduces to:

$$L = \frac{p_e}{p_e + p_\pi} \tag{4.7}$$

The result is between 0 and 1 and basically calculates the electrons fraction of the two probabilities. Each spectrum is normalized to unity and therefore represents the probability density function for the energy deposition of the particle.
The equation also shows that the identification (likelihood) value only depends on the ratio between the probabilities of the two particles to produce a certain energy deposition. This means that the identification primarily works for energy depositions above 10 keV where the TRD is observing the influence of the transition radiation photons.

The probabilities for Eq. 4.7 can be extracted from the mentioned energy deposition distributions of the two particles, which are seen in 4.7 and were made with the usage of MC information. This means, that the simulated tracks were matched to the MC tracks of the simulation which allows for an ideal particle identification. This method is used for the development of an identification method and for simulation studies of the detector. However, the later data taking will need to be able to create clean electron and pion samples via cuts or with the help of the other sub-detectors of the CBM experiment (further discussions will follow in chapter 4.3).

The CBM-TRD features four TRD layers. Each layer measure an individual energy deposition of the same track. The probability for Eq. 4.7 in case of measurements in multiple layers is calculated by:

$$p_e = \prod_{i=1}^{n} p_{e_i} \tag{4.8}$$

Where n is the amount of triggered TRD layers and p_{e_i} is the probability for the energy deposition measured in the respective layer.
Differences of the probabilities in each layer contribute directly to the calculation of the final likelihood value and therefore multiple triggered TRD layers provide multiple chances of measuring an energy deposition above 10 keV. This leads to much larger probabilities for electrons and to a good identification. This indicates a strong dependence of the identification performance on the number of TRD hits (number of triggered layers).
Around 50% of primary electron tracks trigger all the four TRD layers (see Fig. 4.8).

As the TR depends on the momentum and the identification of the TRD is getting more powerful for momenta above 1 GeV one can investigate the momentum dependant performance of the likelihood method. Figure 4.9 shows the energy deposition spectra for three momentum intervals. The spectrum in the top left is in the region of p=0-1 GeV/c and therefore does not include a significant amount of transition radiation photons. It is still possible to do particle identification in this momentum region, because of the differences in the specific energy loss of the electrons in comparison to the pions, but it is not as powerful as in the momentum regions that include TR photons.
The spectrum in the top right shows the momentum region of p = 1-3 GeV/c and one can see the influence of the TR photons which produce significantly higher probabilities for larger energy depositions.

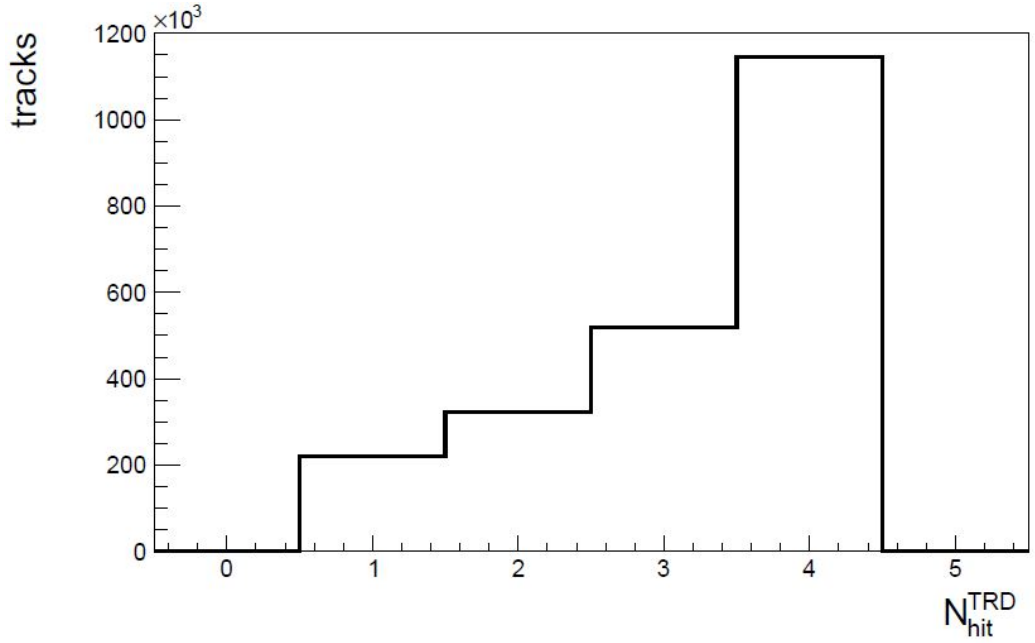

Figure 4.8: Distribution of different numbers of TRD hits for MC matched primary electron tracks.

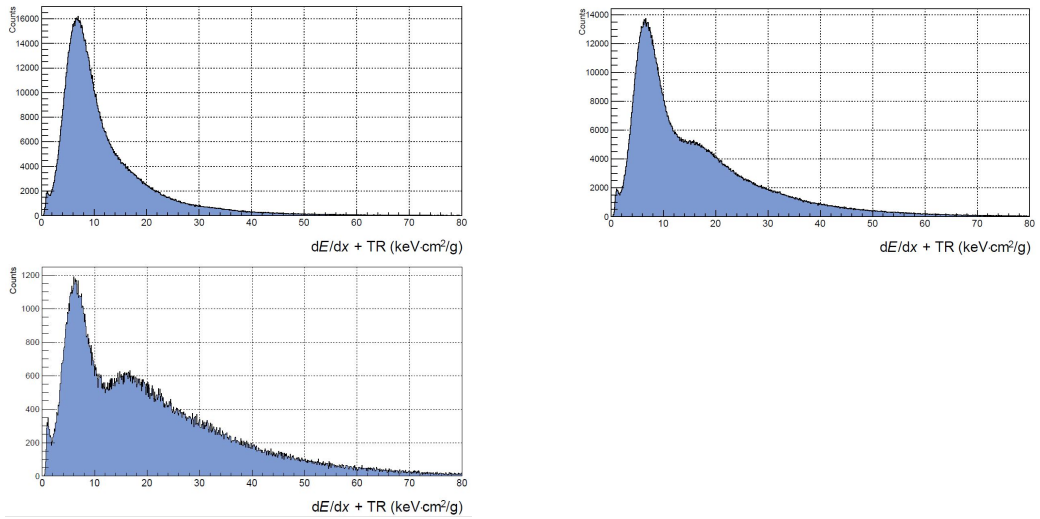

Figure 4.9: Energy deposition spectra for MC matched primary electrons and for different momentum regions. Top left: p=0-1 GeV/c Top right: p=1-3 GeV/c Bottom left: p=3-20 GeV/c

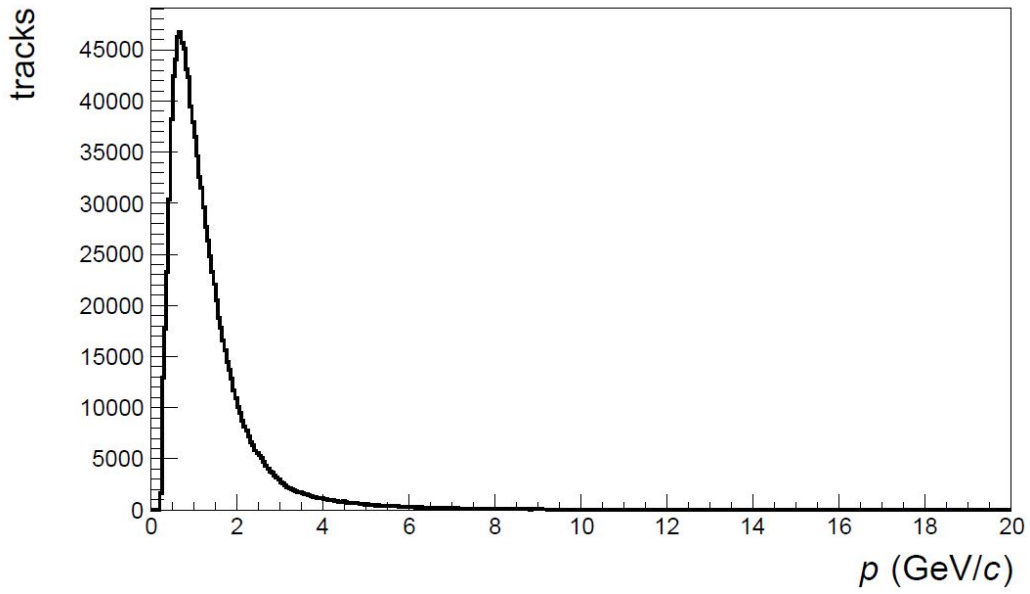

Figure 4.10: Momentum distribution for the reconstructed primary electron tracks.

The last spectrum is in the momentum region of p = 3-20 GeV/c and therefore shows the full effect of the TR photons on the spectrum. The momentum region is also the largest interval of these three but the statistics are comparably low because of the underlying momentum distribution (see Fig. 4.10).

The momentum dependent character of the transition radiation leads to the fact that the probability distributions for the likelihood method should also be momentum dependent in the optimal case. Figure 4.11 shows an example of such an distribution. The usage of a momentum dependent distribution improves the precision of the likelihood values especially for the lower momentum region. To extract the probabilities for Eq. 4.8 and 4.7 one needs to normalize the two dimensional distributions for every momentum interval individually to unity. Afterwards the projections for the respective momenta will look like the spectra in Fig. 4.7 and the probabilities can be read off at the point of the measured energy deposition. The binning has to be chosen in a way that there is sufficient statistics for the momentum projections. On the other side its granularity should be fine enough to capture the momentum dependant variations of the shape.

The number of triggered TRD layers also strongly influences the perfor-

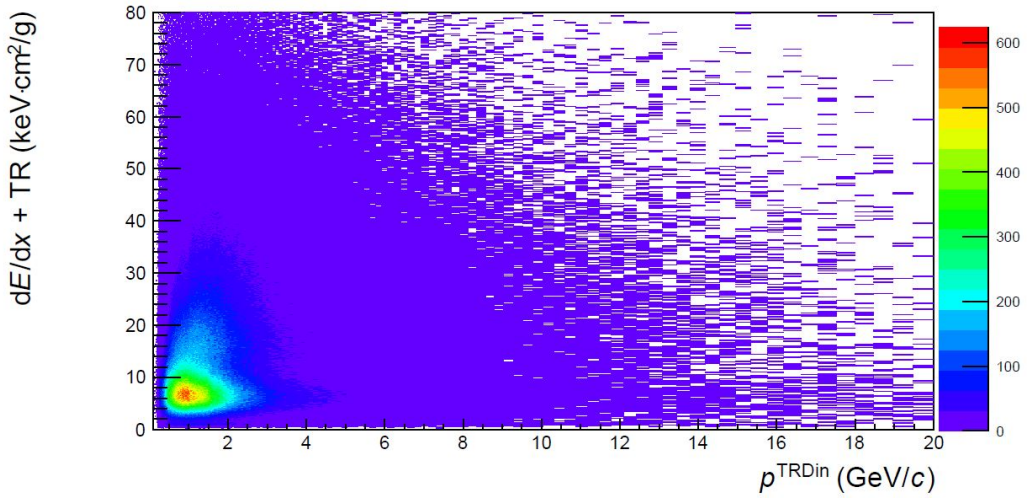

Figure 4.11: Momentum dependent energy deposition distribution for primary electrons identified via the MC matching method.

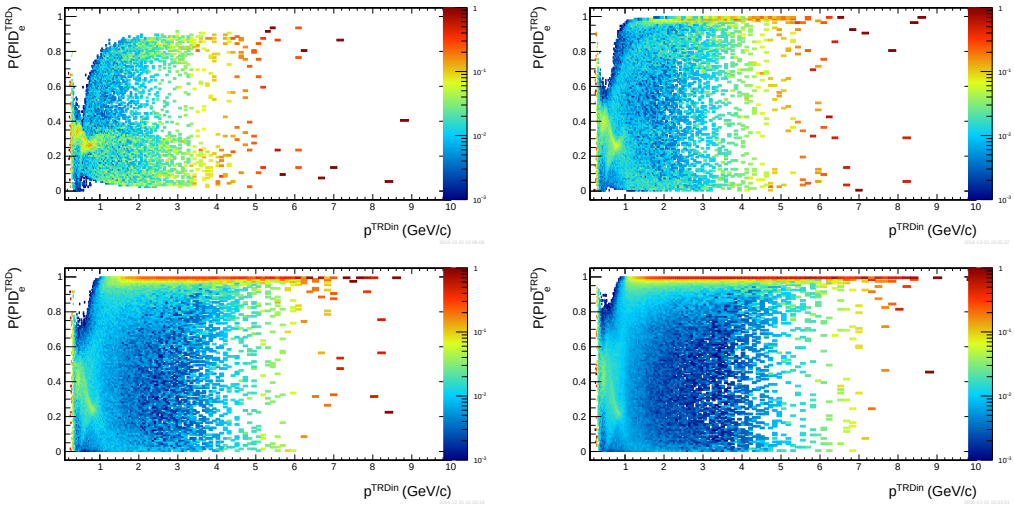

Figure 4.12: Comparison of the momentum dependent likelihood values for MC matched primary electrons and for different numbers of triggered TRD layers normalized to unity for every momentum bin and shown on logarithmic scale. Top left: 1 Hit Top right: 2 Hits Bottom left: 3 Hits Bottom right: 4 Hits.

mance of the particle identification. Figure 4.12 is showing a comparison of the influence of different numbers of TRD hits to the likelihood method. The method was used on primary electron tracks which were identified via the MC matching method. In the top left panel one can see the plot for tracks that only produced one TRD hit. This histogram has the lowest amount of statistics and also a very low average probability value for being an electron track. Even in the momentum region above p = 3 GeV/c where the identification of electron tracks should be easiest the identification has large fluctuations. This can be explained through the most probable energy deposition of electron tracks in this momentum region as shown in the bottom left of Fig. 4.9. The maximum can be found around 8 keV, but in the region of such energy depositions the probability for pions is even larger (see Fig. 4.7). Because of this the identification can only be successful if the track is showing the influence of TR, but this is not likely to happen in every one hit track. Therefore the likelihood value is showing large fluctuations since the value becomes either large for energy depositions that include a TR photon or very low for those which do not, since for low energy depositions it is far more probable to be a pion.

This effect reduces drastically with multiple TRD hits as one can see in the other panels, because it is much more likely to measure TR for a track with multiple triggered TRD layers. With two TRD hits (top right panel of Fig. 4.12) the identification results already improve significantly and with three (bottom left panel) and four hits (bottom right) one can see a red line around 1 which indicates that the vast majority of tracks above a momentum of p = 2 GeV/c receives a clear identification. The difference between three hits and four hits is relatively minor, which allows the usage of three and four hit tracks for the analysis.

Figure 4.13 is showing the probability distribution for electrons determined for different numbers of hits integrated over all momenta and normalized to unity. The one hit tracks (black) and the two hit tracks (red) have their maximum values for low identification probabilities and therefore these tracks are not useful in the analysis. The three (green) and four (blue) hit tracks both have their maximum around the value one. Qualitatively they perform relatively similar but quantitatively is the identification for four TRD hits superior as one would expect. For practical usage one does include three and four hit tracks since the restriction on pure four hit tracks would reduce the statistics in the analysis.

The cut on the likelihood value determines the statistics provided for an

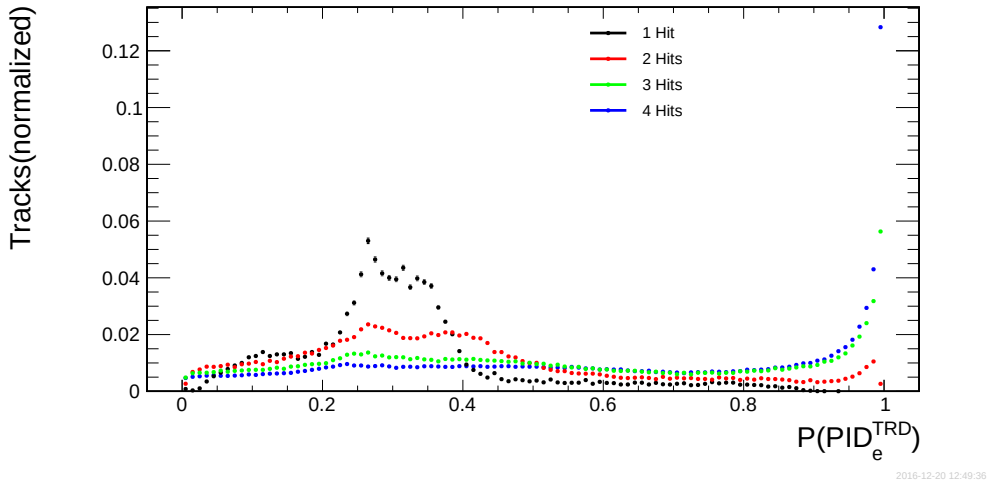

Figure 4.13: Likelihood value for MC matched primary electrons and for different numbers of measured hits in the TRD integrated over all momenta.

analysis and is typically set to a certain electron efficiency (the percentage of included electrons after identification cuts). This can be done momentum and number-of-hit dependent. The selected electron efficiency influences the statistics, the purity of the signal and also the pion suppression (further discussion in Chap. 5).

4.4 V0-Topology analysis for the creation of electron and pion samples

Like the ANN the likelihood method needs some sort of training data, which is given by the mentioned probability density functions of the energy deposition. These are easily provided with the help of MC matching, but for the later data taking one needs to be able to create pure electron and pion samples via other tools than MC information. For this purpose one can use so-called *V0-Topologies* which are a specific group of pair decays.

4.4.1 Overview of V0-Topologies

The name V0-Topologies refers to their characteristic appearance. The decay group describes a pair decay with two contrarily charged daughter particles, which are produced in the decay of a short living, neutrally charged mother

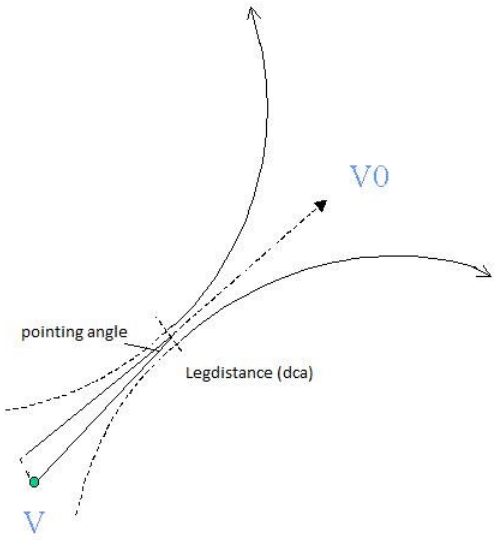

Figure 4.14: Sketch of a V0-Topology with the primary vertex, the pointing angle and the leg distance.

particle. The neutral mother particle is produced at the *primary vertex* and can not be detected directly, but one can measure the charged daughter particles in the detector which are produced at the *secondary vertex* (see Fig. 4.14). In this sketch the primary vertex is indicated by the green point and the secondary vertex is shown in the middle of the leg distance. Since one can not see the mother particle one has to reconstruct its primary vertex via the masses and momenta of the daughter particles. The vector of the momentum sum should point to the primary vertex.
Typical V0-Topologies include the decay of the γ, K_S^0 ($= \frac{1}{\sqrt{2}}(K_0 + \bar{K_0})$), $\bar{K_S^0}$, Λ and the $\bar{\Lambda}$ [Par16].

mother particle	dominant decay channel	secondary decay channel
Λ	p π^-	nπ^0
	BR= (63.9 $\pm$ 0.5)	BR= (35.8 $\pm$ 0.5)
$\bar{\Lambda}$	$\bar{p}$ π^+	nπ^0
	BR= (63.9 $\pm$ 0.5)	BR= (35.8 $\pm$ 0.5)
K_S^0	$\pi^+\pi^-$	$\pi^0\pi^0$
	BR= (69.2 $\pm$ 0.05)	BR= (30.69 $\pm$ 0.05)
$\bar{K_S^0}$	$\pi^+\pi^-$	$\pi^0\pi^0$
	BR= (63.9 $\pm$ 0.5)	BR= (30.69 $\pm$ 0.05)
γ	e^+e^-	
	($\sim$ 100)	

From these decays $K_S^0 \to \pi^+\pi^-$ can be used to create a pion sample and the γ-conversion provides one for the electrons.

To identify these decays one can use several track and pair variables which are defined for pair decays.
These include:

Distance to the primary vertex — Distance in propagation direction of the mother particle between the secondary and the primary vertex.

R — The variable **R** also refers to the distance between the primary and the secondary vertex but with the distance in the plane orthogonal to the beam propagation.

Opening angle ϕ — The opening angle describes the angle between the tracks of two daughter particles defined at the secondary vertex.

Pointing angle θ	The pointing angle refers to the angle between the line connecting primary and secondary vertex and the vector of the momentum sum (see Fig. 4.14) .
DCA	The ***D**istance of **C**losest **A**pproach* (DCA) or also called *leg distance* in this analysis is the closest distance of the reconstructed tracks of the daughter particles (see Fig. 4.14).
χ^2/NDF rel to the primary Vertex	The χ^2-value is part of probability theory. It refers to the probability of the measured tracks to fit to the primary vertex. The higher the value is the more unlikely it is for the track to originate from the vertex. The NDF stands for *number of degrees of freedom* which is typically 3.
Φ_v	The Φ_v variable describes the angle between the decay plane and the plane orthogonal to the magnetic field.
Armenteros Podolanski variables	These variables depend on the masses and momenta of the daughter particles as well as their transverse momentum. They show a specific behaviour for the different decays mentioned before and will be further explained later.

These variables have to be investigated and optimized for their ability to identify the decays into pions and electrons to create a good combination of purity in the samples and enough statistics.

4.4.2 Cut investigation

To create pure electron and pion samples the mentioned variables have to get analysed with respect to their capabilities to identify the different decays. To optimize the cut settings one has to get an overview of the general distributions of the variables for the different decays.

Reconstruction cuts on the tracks which were always included are:

	Variable	Cut values
Acceptance cuts	P_t	$\geq$0.05 GeV/c
(MVD+) STS reconstruction cuts	Number of MVD+STS Hits	6 - 15
TRD reconstruction cuts	Number of TRDHits	1 - 4

One can separate the cut groups into two configurations. One configuration is dedicated to create pion samples and one should provide electron samples.

A cut that can be defined for those two configurations separately is the invariant mass. The mother particles, i.e. the γ and the K^0_S, have different masses, e.g. the kaon mass is 497.614 ± 0.025 MeV/c^2. This can be used to create an invariant mass range around the known kaon mass.
The γ-conversion has an invariant mass of 0 but is selected within a mass range up to 50 MeV/c^2, due to resolution.
The variable distributions also include a combinatorial background (xx (comb)) which contains all pair candidates. It includes all kinds of two body decays, as well as primary particles that come very close and can be misidentified as a pair.
The variable distributions are shown with the cut positions of the later used cut groups. The separation of the cuts into groups and their position are explained in the separate *pion configuration* and *electron configuration* chapters.

Opening angle
Figure 4.15 is showing a comparison of the opening angle distributions for the different V0-decays, while also including a distribution for the combinatorial background (here to see as xx (comb)). The distributions are logarithmically drawn and normalized to unity to compare their shape. As one can see, pair conversions are located at very small opening angles, which is due to the low masses of the two daughter particles. Nearly 80% of the conversions are in the first bin which indicates that the opening angle could be a useful tool for the selection of electron samples. The combinatorial background shows a lower amount of small opening angles and has a maximum around 0.3 rad.

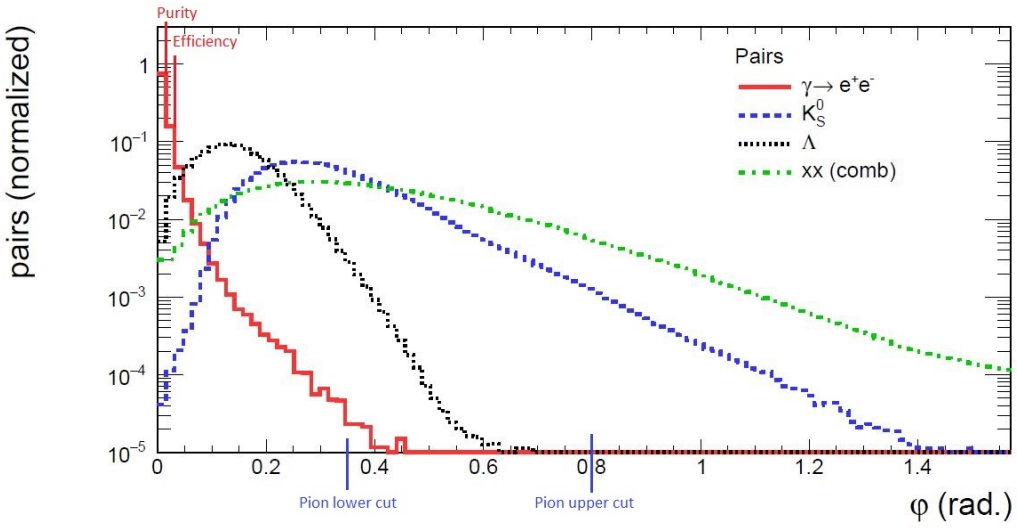

Figure 4.15: Comparison of the opening angle distributions for the different V0 decays, also including a combinatorial background (xx (comb)).

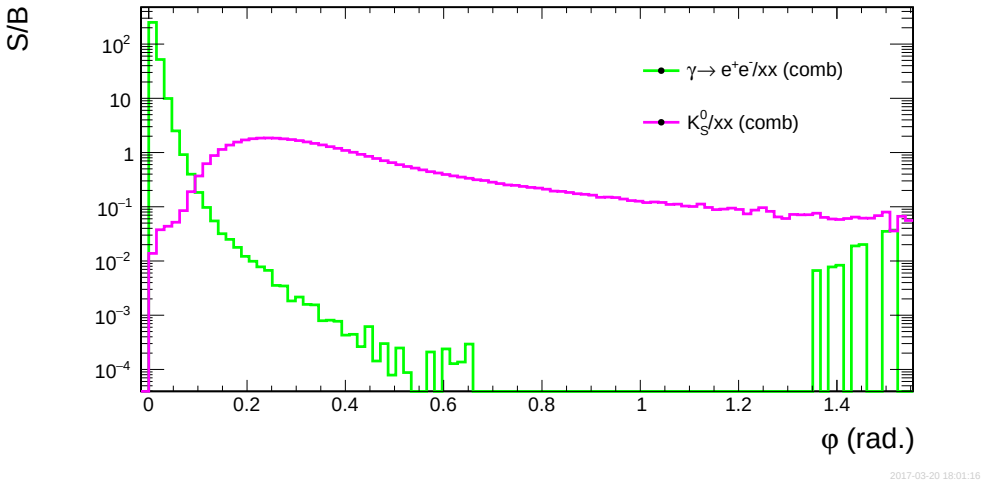

Figure 4.16: Comparison of the signal-to-background ratios of the γ and the K^0_S decays as a function of the opening angle.

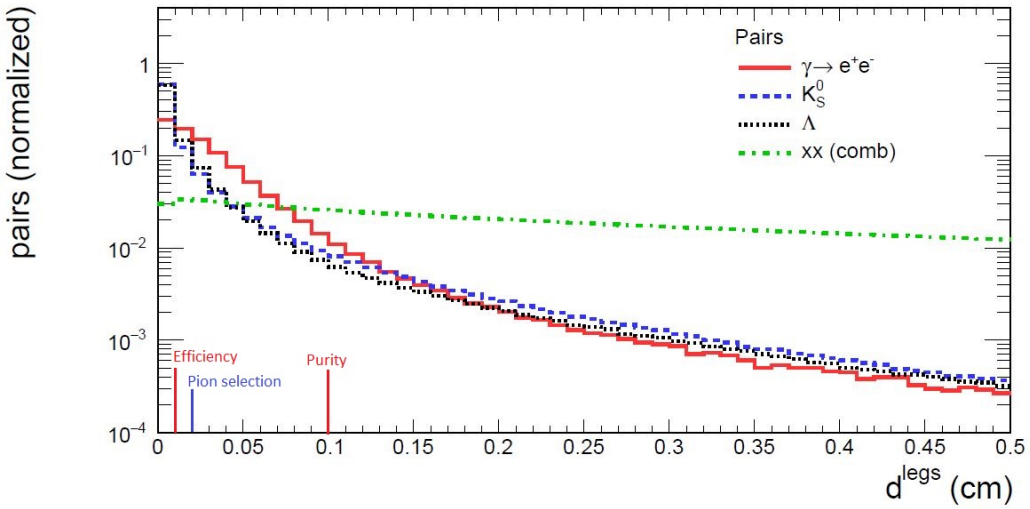

Figure 4.17: Comparison of the leg distance distributions for the different V0-decays also including the combinatorial background (xx (comb)).

The K^0_S-decay has a less significant maximum. The distribution overlaps with the others, which leads to a worse signal-to-background ratio which can be seen for both decay channels in Fig. 4.16. The ratio is calculated for the specific decays in comparison to the combinatorial background ($\gamma \rightarrow e^+e^-$/xx (comb) and K^0_S/xx (comb)). It shows the good ratio for the conversions at small opening angles and higher values for the K^0_S channel between 0.2 and 0.4 rad.

Leg distance (DCA)

The leg distance or DCA should be small for V0-decays. In Fig. 4.17 the normalized distributions for the different V0-decays are shown. All three V0-decays show the same behaviour with smaller leg distances. Only the combinatorial background differs from that behaviour which is indicating that one can use this variable to reduce the combinatorial background without affecting the signals drastically. Figure 4.18 shows the signal-to-background ratios for the decay channels with significant ratios for the suppression of the combinatorial background. The γ-conversion shows the smallest maximum value in the first bin. The main use of the variable is the reduction of the combinatorial background.
In general, the same holds for the K^0_S-decay but since the maximum value is larger by more than a factor two in comparison to the conversions, the K^0_S has a better signal-to-background ratio.

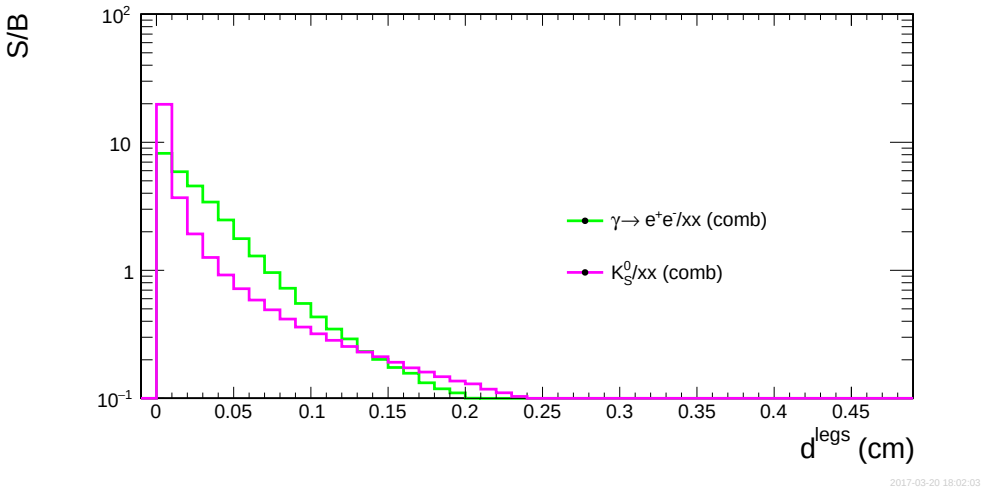

Figure 4.18: Comparison of the signal-to-background ratios of the γ and the K^0_S decays as a function of the leg distance.

Pointing angle

The pointing angle refers to the difference between the connection of the primary and the secondary vertex and the vector of the momentum sum of the daughter particles. It should be a very small angle for V0-decays. The distributions of the different decays show a comparable behaviour as one can see in Fig. 4.19. The distributions are again normalized and one can also see the difference between the V0-decays and the combinatorial background.
Similar to the behaviour of the leg distance the pointing angle also offers a tool to reduce the combinatorial background. Figure 4.20 shows this background suppression capabilities.

Distance in the xy-plane between the primary and the secondary vertex

The distributions of the distance in the xy-plane (the plane orthogonal to the direction of the beam line) can be seen in Fig. 4.21. All the distributions are trending towards the zero but with different shapes and positions of their maxima. The γ conversion have their maximum at the largest value and they also have the widest distribution of the shown shapes. Still, they exhibit a large overlap with the other decays and therefore they can not be separated from the other V0 decays via a cut on this variable, but it can be used with lower and upper cut to reduce the combinatorial background (see Fig. 4.22). The K^0_S-decays on the other hand do overlap with the rest of the shapes

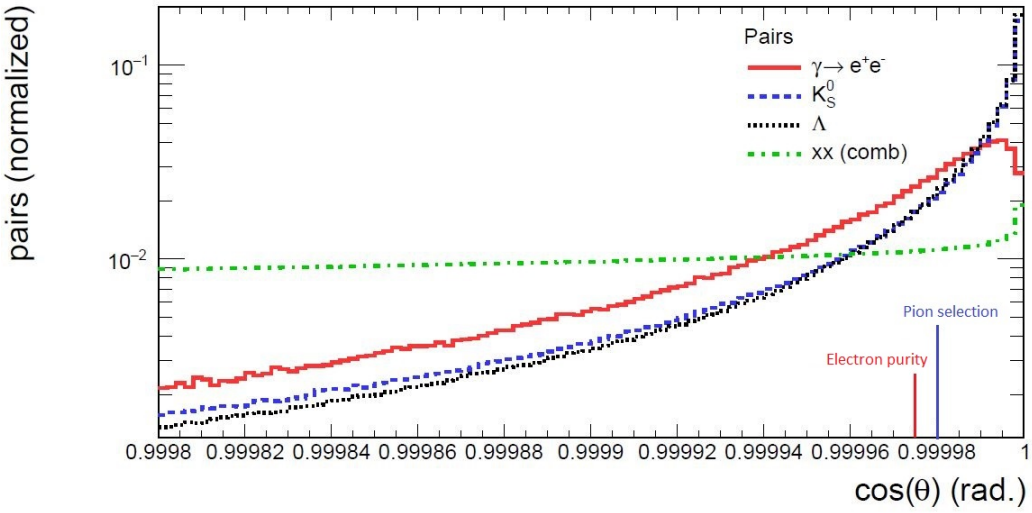

Figure 4.19: Comparison of the pointing angle distributions for the different V0-decays also including the combinatorial background (xx (comb)).

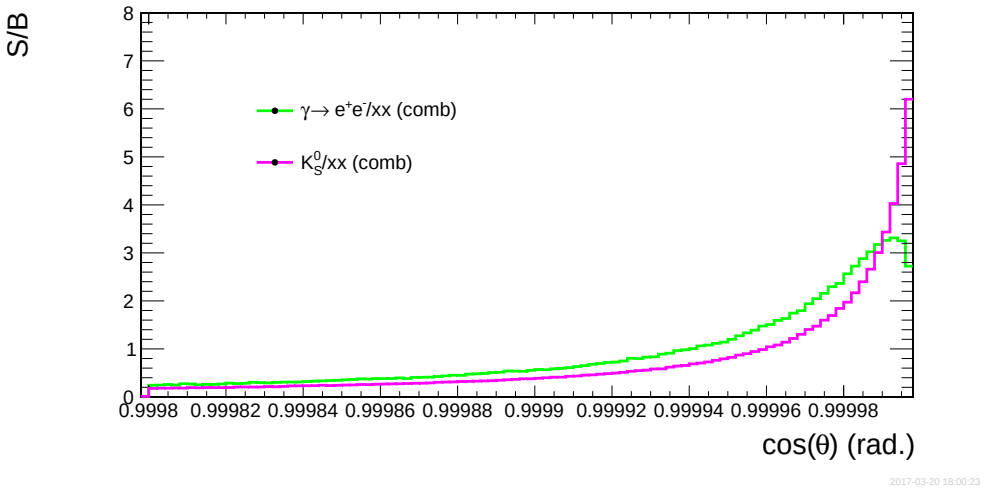

Figure 4.20: Comparison of the signal-to-background ratios of the γ and the K^0_S decays as a function of the pointing angle.

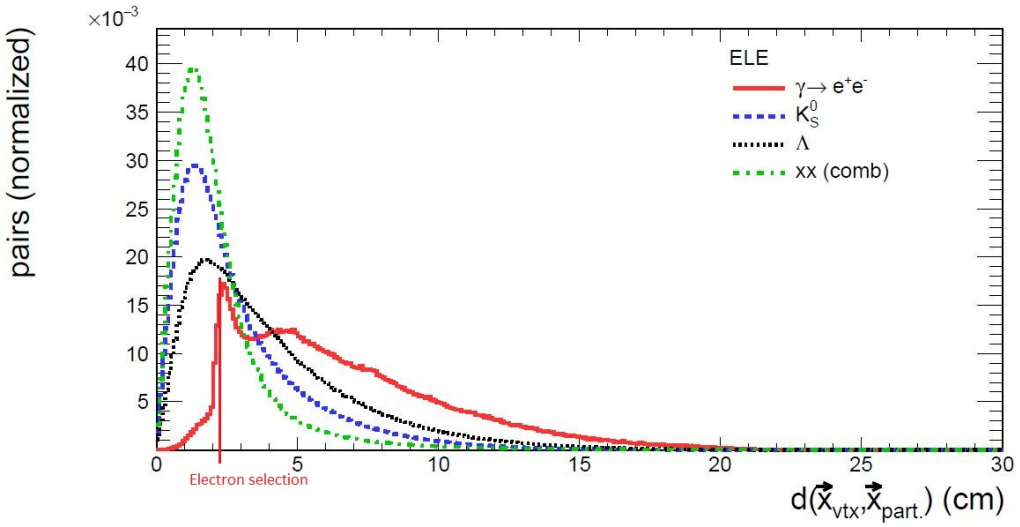

Figure 4.21: Comparison of the distance in the xy-plane between the primary and the secondary vertex for the different V0-decays also including the combinatorial background (xx (comb)).

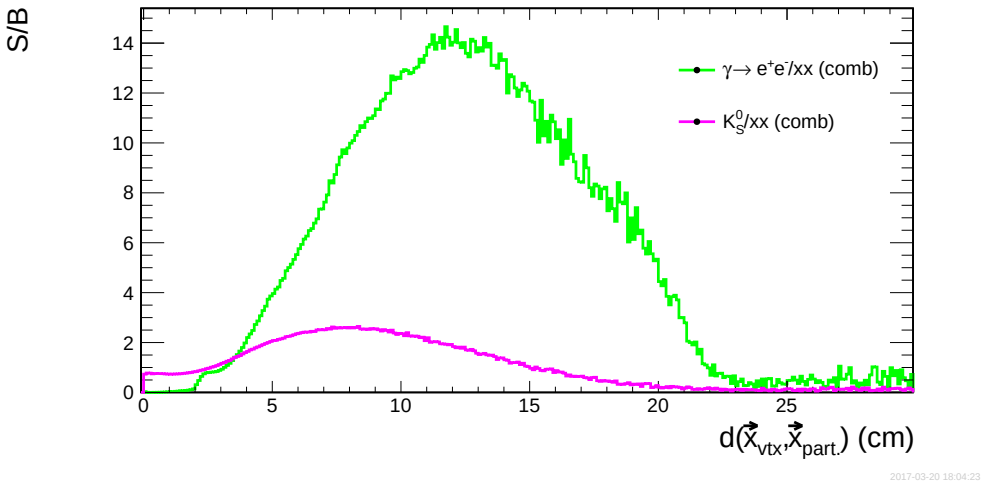

Figure 4.22: Comparison of the signal-to-background ratios of the γ and the K^0_S decays as a function of the xy-plane.

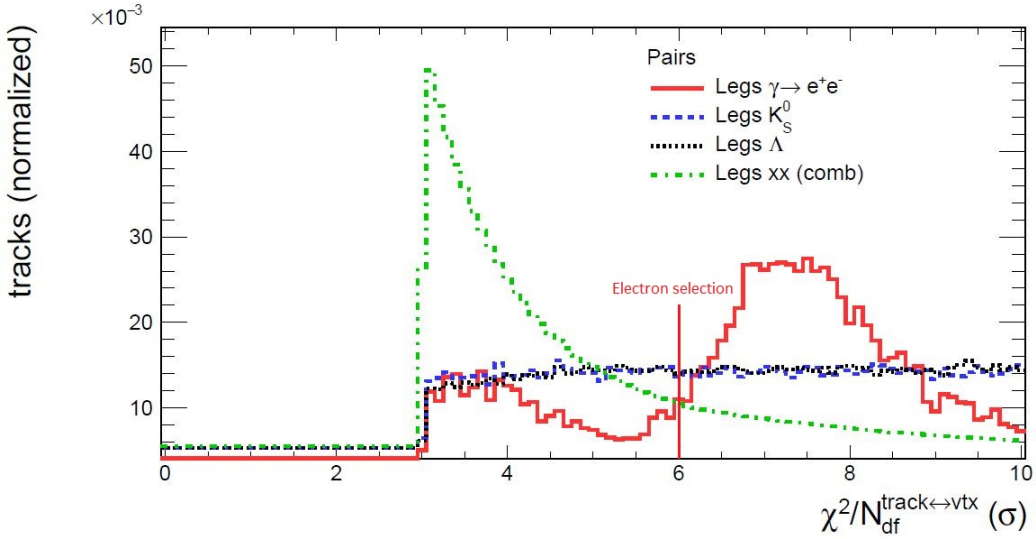

Figure 4.23: Comparison of the probability indicator χ^2 as track parameter for conversions, kaon decays and combinatorial background xx.

and especially with the combinatorial background, so there is no significant background rejection by this cut.

χ^2/NDF to vertex

Figure 4.23 shows the χ^2 distributions for the V0-decays and the combinatorial background. Values below 3 are rejected because these are tracks which are pointing to the primary and not the secondary vertex. Values above 10 are also rejected since these would be bad V0 candidates. As one can see the conversions have a clear maximum in the range of 6-10. The second little local maximum around 3.5 is not significant so the interesting region for further conversion selection lies between 6 and 10. Figure 4.24 shows again the corresponding signal-to-background ratios with the background rejection for the conversion selection in green.
The kaon decay has no maximum and can not be selected with this cut.

The Φ_v angle

The Φ_v angle is a variable of special interest for V0-decays. It is defined for two body decays and is expected to show a specific behaviour for the conversions in contrast to the other signals.

In Figure 4.25 one can see a sketch of a V0-decay with the daughter particles, their opening angle between them and the magnetic field. The decay plane is shown in orange and the plane orthogonal to the magnetic field is

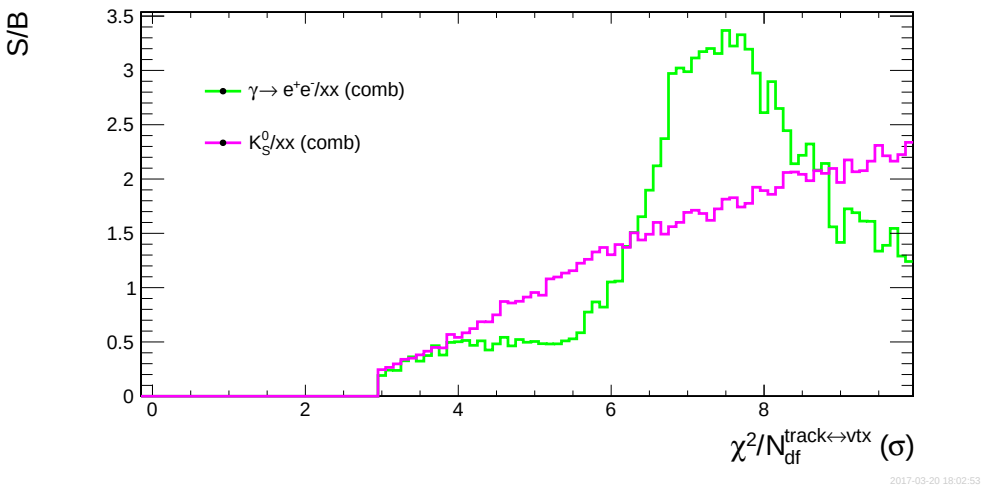

Figure 4.24: Comparison of the signal-to-background ratios of the γ and the K_S^0 decays as a function of the χ^2.

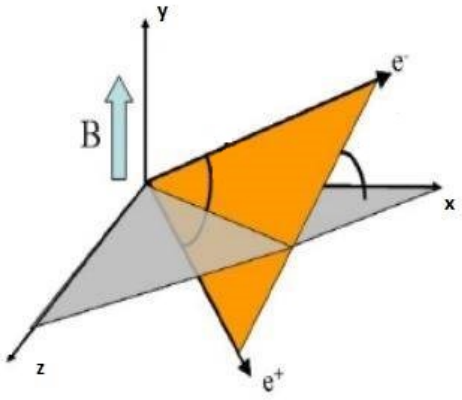

Figure 4.25: Sketch of the decay plane (orange), the magnetic field (B),the plane orthogonal to the magnetic field (grey) and the Φ_v angle.

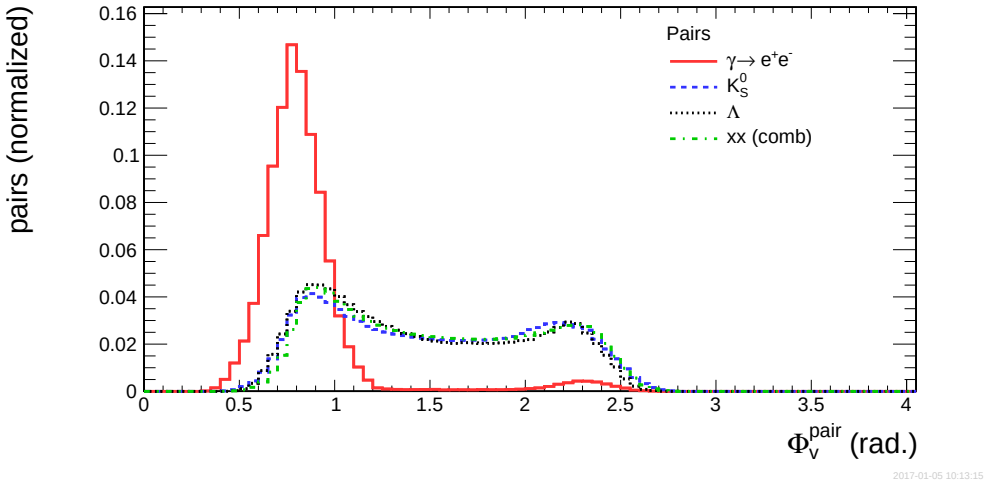

Figure 4.26: Comparison of the Φ_v angle distributions for the different V0-decays also including the combinatorial background (xx (comb)).

displayed in grey. Φ_v is the angle between these two coloured planes.

It is calculated from the momenta of the daughter particles and the magnetic field direction. Here $\vec{b}$ is the unity vector of the magnetic field in the direction of the y-axis, $\vec{p_1}$ and $\vec{p_2}$ are the momenta of the daughter particles and $\vec{n}$ is the unity vector orthogonal to the decay plane. Φ_v is thus defined as:

$$\vec{n} = \frac{\vec{p_1} \times \vec{p_2}}{|\vec{p_1} \times \vec{p_2}|} \tag{4.9}$$

$$\Phi_v = \cos^{-1}\left(\frac{\vec{b} \cdot \vec{n}}{|\vec{b} \cdot \vec{n}|}\right) \tag{4.10}$$

Figure 4.26 shows the behaviour for the Λ, K_S^0 and the combinatorial background are the same, while the conversions has a different shaped distribution with a comparably narrow maximum between 0.4 and 1.2 rad. The other decays are distributed over the region between 0.5 and 2.7 rad. They have two local maxima which however are not very pronounced. A cut on this variable will improve the conversion selection without strongly affecting the statistics of the electron samples.

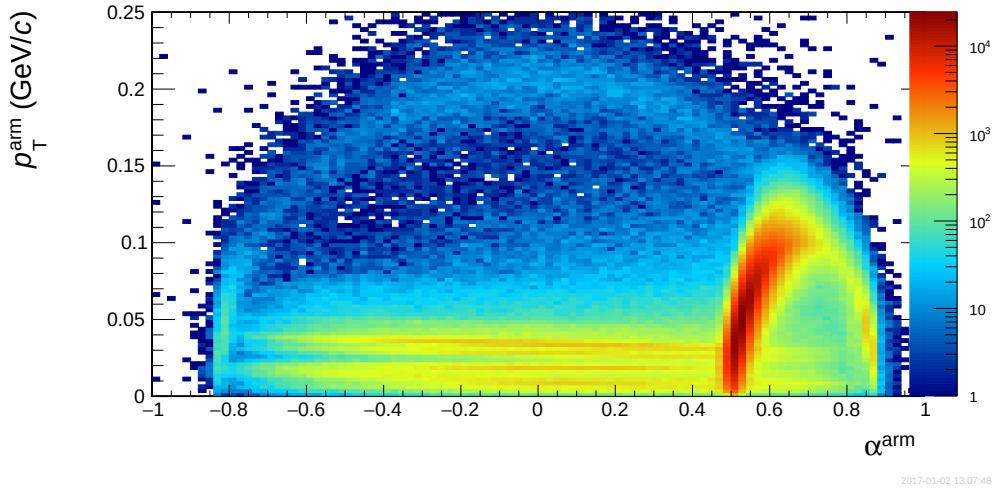

Figure 4.27: The Armenteros-Podolanski plot including γ-conversions, K^0_S- and Λ-decays.

Armenteros Podolanski variables/plot

The *Armenteros Podolanski plot* or sometimes just called *Armenteros plot* is a two dimensional plot which shows the correlation between the transverse momentum of the positive daughter particle (p_T^{arm}) and the momentum of the reconstructed mother particle and a variable which corresponds to the momentum symmetry of the decay (α^{arm}).

$$p_T^{arm} = \sqrt{-\left(\frac{\alpha^{arm} - \alpha_0}{r_\alpha}\right)^2 \cdot p_{cms}^2} \tag{4.11}$$

$$\alpha^{arm} = \frac{p^+ - p^-}{p^+ + p^-} \tag{4.12}$$

with:

$$r_\alpha = \frac{2 \cdot p_{cms}}{M} \tag{4.13}$$

$$\alpha_0 = \frac{m_+^2 - m_-^2}{M^2} \tag{4.14}$$

Where p_{cms} is the momentum in the center of mass system, m^+ and m^- are the masses of the positively and negatively charged daughter particles and M is the mass of the mother particle.

An example of the correlation between the two variables is shown in Fig. 4.27. This plot includes signals from γ-conversions, K_S^0, Λ and $\bar{\Lambda}$-decays, although the $\bar{\Lambda}$-decays have very low statistics.

In the plot one can see different characteristic elliptic shapes. The γ-conversions are primarily found in the region below 0.05 p_T^{arm}. The Λ-decay is the clearly defined ellipse at the right side of the plot and the K_S^0-decays are seen as a wide, less distinct ellipse in the upper half. The $\bar{\Lambda}$-decay distribution is mirrored with respect to the one of the Λ on the left side, but is not significantly visible because of low statistics. All the decays will be shown as individual Armenteros Podolanski plots in the further cut optimization.

The reason why the Λ and the $\bar{\Lambda}$ sit on the right, respectively left, side of the plot is because of their asymmetric decay pattern. The γ-conversion and the K_S^0 both decay into two daughter particles of the same mass. The Λ and the $\bar{\Lambda}$ both decay into two daughter particles with a mass difference of approximately 800 MeV/c^2.

The different characteristic elliptic shapes of the decays can be described via a simple ellipse equation which uses the information of the momenta and masses of the decay participants. The ellipse is defined as:

$$\left(\frac{\alpha^{arm} - \alpha_0}{r_\alpha}\right)^2 + \frac{p_T^2}{p_{cms}^2} = 1 \tag{4.15}$$

α_0 describes the position of the center of the ellipse and p_{cms} modifies the semi-major axis of the ellipse.

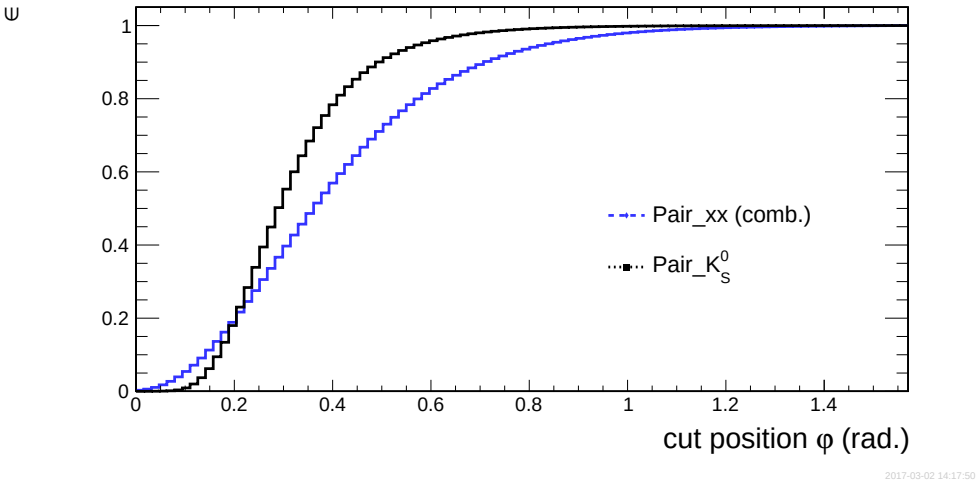

Figure 4.28: Signal efficiencies for the K^0_S-decays and the combinatorial background depending on the cut position of the opening angle.

4.4.3 Pion configuration

A closer look on the impact of different cut positions delivers further information for the selection of pion samples via the K^0_S decay channel. The invariant mass already provides a powerful selection criterion so that the remaining identification cuts do not have to be selected in the most strict way and still produce a relatively pure sample.

To investigate the cut configuration a useful tool is the signal efficiency depending on the cut position. This efficiency describes the fraction between the decays which are reconstructed and the decays which are accepted by the topology cuts depending on the cut values ($\frac{\text{accepted pairs}}{\text{reconstructed pairs}}$). The efficiency is either calculated for a lower cut limit or for an upper cut limit depending on the position of the maximum and the behaviour of the variable. The amount of accepted pairs is then defined as the pairs between the minimal possible value and the upper cut limit (for example for the opening angle) or the maximal possible value and the lower cut limit (for example for the pointing angle).

Figure 4.28 shows the comparison of the efficiencies for the K^0_S-decay and the combinatorial background depending on the upper cut on the opening angle. As one can see the difference is not very significant. Through calculation of the ratio in each bin one can find the best signal-to-background ratio

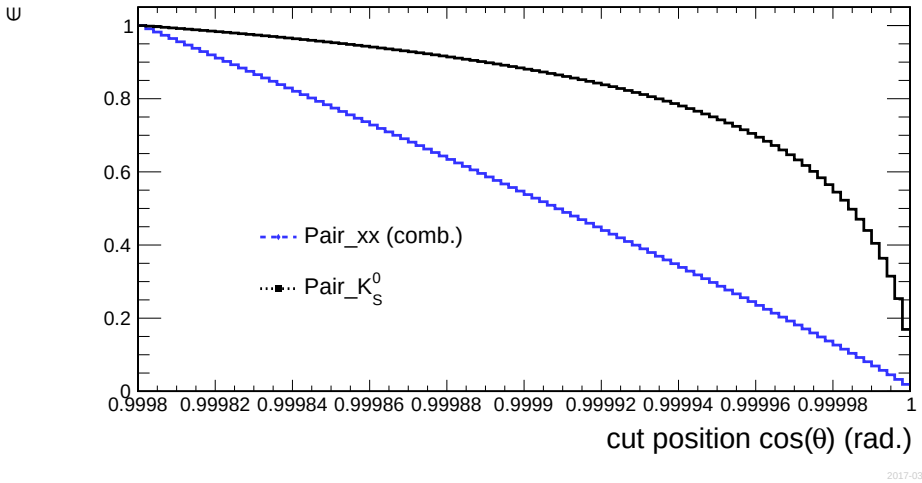

Figure 4.29: Signal efficiencies for the K^0_S-decays and the combinatorial background depending on the cut position of the cosine of the pointing angle.

between the opening angles of 0.35 and 0.8 rad. The upper limit does not reject a huge amount of the remaining K^0_S signal but the lower limit does reject about half of the signals. This can be adjusted depending on the statistical needs but in our case the pion sample efficiency is not as important as its purity.

The cosine of the pointing angle is showing a larger difference in the efficiency for kaon-decays and background (see Fig. 4.29). The best signal-to-background ratio is found for a cosine value of 0.99998. This lower cut provides a good signal-to-background ratio combined with a good efficiency.

The leg distance is shown in Fig. 4.30. It has a very high signal-to-background ratio. If one uses an upper cut on the value 0.02 one is getting a background suppression of a factor 10 while still keeping 72% of the kaon signal.

The last investigated cut for the K^0_S-decays in this analysis is the cut on the Armenteros Podolanski ellipse which was mentioned in Chap. 4.4.2. With usage of Eq. 4.5 one can calculate the theoretically ideal Armenteros-Podolanski ellipse produced in K^0_S-decays. In reality this ideal ellipse will be smeared out due to fluctuations and therefore show a wider distribution. Basically, the Armenteros-Podolanski plots are another cut on the invariant mass, but they can be used to reduce the ambiguity between K^0_S and $\Lambda+\gamma$.

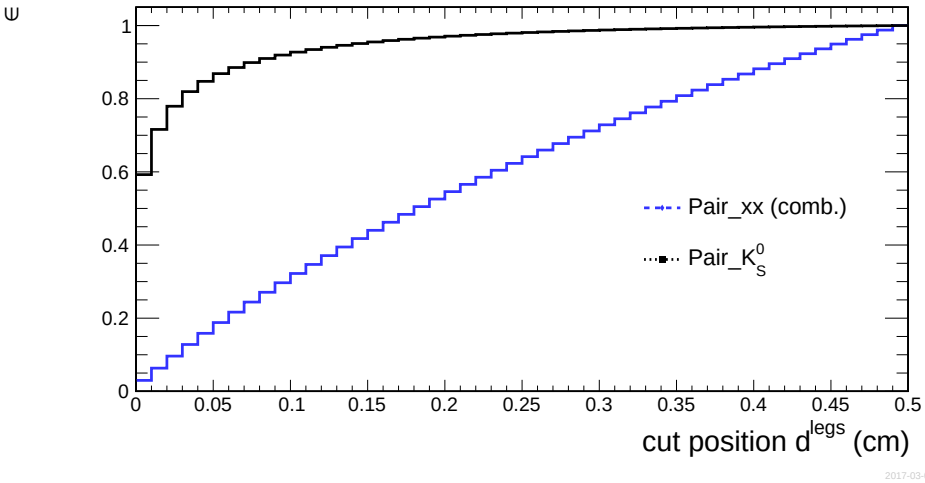

Figure 4.30: Signal efficiencies for the K^0_S-decays and the combinatorial background depending on the cut position of the leg distance.

Figure 4.31 is showing the result of this variation drawn into a plot of MC matched kaon decays. The functions of the ellipse variations can be used as α_{arm} dependent cuts.

The concluding cut configuration then looks like this:

cut variable	minimum value	maximum value
OpeningAngle	0.35 (rad.)	0.8 (rad.)
Cos(PointingAngle)	0.99998	1.0
Leg distance	0.0	0.02
Invariant mass	0.4971 (GeV/c^2)	0.4981 (GeV/c^2)

The result then produces a very pure pion sample as one can see in Fig. 4.32, which is showing all the pairs in the sample in red and the pions originating from K^0_S in blue.

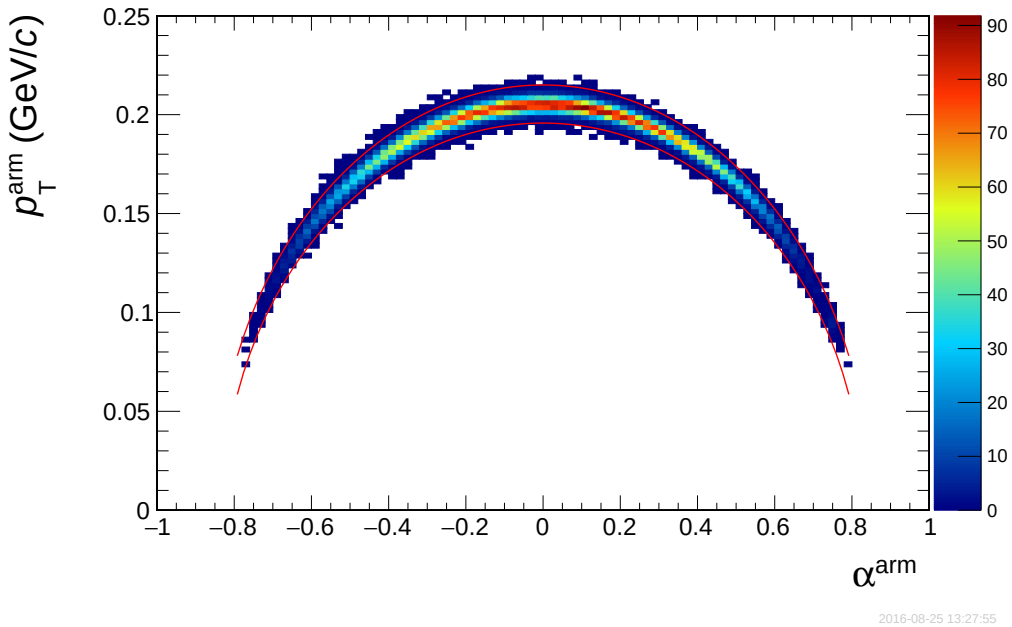

Figure 4.31: Armenteros-Podolanski plot for MC matched K^0_S-decays and drawn with the Armenteros-Podolanski ellipse with variations in the used momenta and masses.

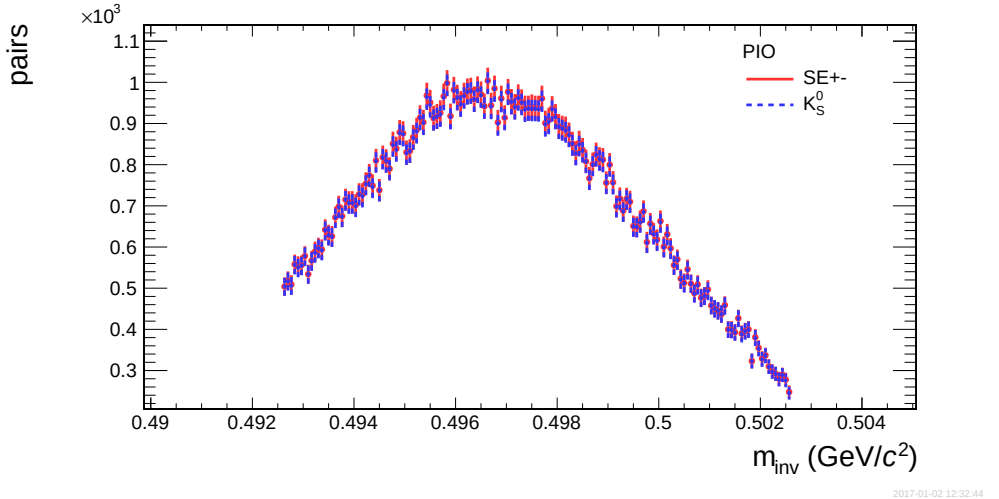

Figure 4.32: Purity of the selected pion sample shown in the invariant mass spectrum with the complete sample in red and the K^0_S in blue.

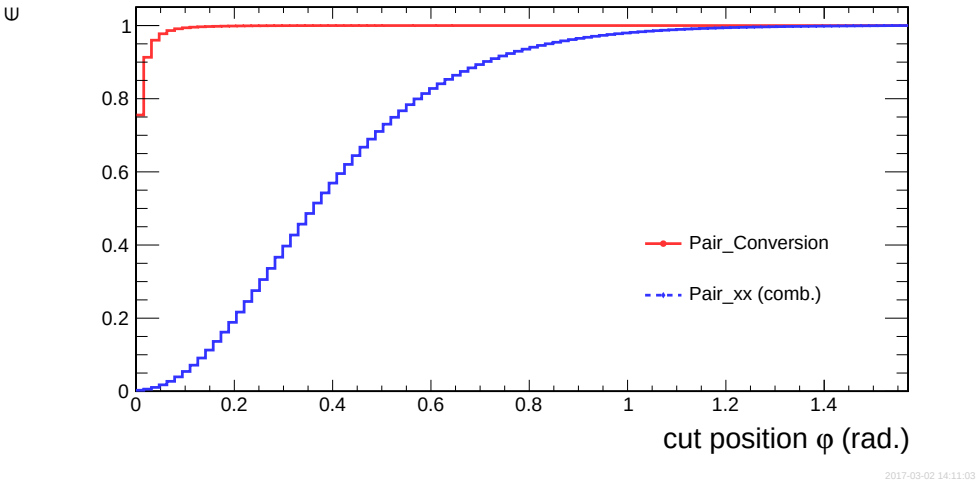

Figure 4.33: Integrated signal efficiencies for the γ-convserions and the combinatorial background depending on the upper cut position of the opening angle.

4.4.4 Electron configuration

For the creation of electron samples the same strategy has been applied but because of the lower statistics of the γ-conversions one has to carefully find a compromise between the purity and the size of the sample. At least for this simulation it is not yet possible to create a momentum dependent probability distribution due to statistics. Even the momentum integrated energy deposition distributions show fluctuations especially in the higher momentum region. This affects the performance of the likelihood method. The usage of additional sub-detectors is only able to compensate the lower momentum region.
To further improve the understanding of the effect of the different cuts the electron configuration will be divided into different sub-cut-groups with the purpose to investigate purity and performance limits.

The opening angle, as also shown in Fig. 4.15, is a very promising cut variable for the conversion selection, because of the low masses of the two daughter electrons which lead to a small opening angle. The opening angle is showing a very strict and distinct maximum near zero and therefore provides a good signal-to-background ratio for small values as one can see in Fig. 4.33 and therefore has a very high efficiency at low values.
The best signal-to-background ratio for this variable can be found in the

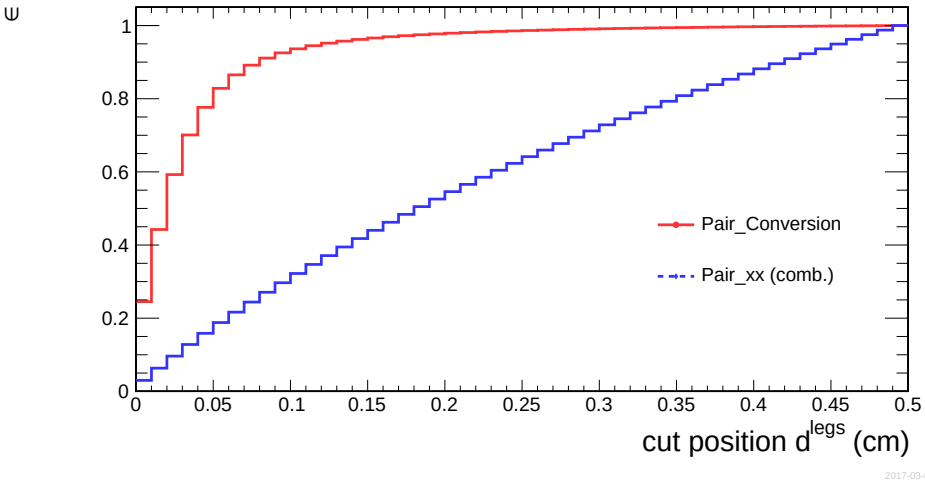

Figure 4.34: Signal efficiencies for the γ-conversions and the combinatorial background depending on the cut position of the leg distance.

first bin since the amount of combinatorial background is very low, but also nearly 25% of the signal would be rejected with a cut on the maximum value of 0.01 rad. With a value of 0.03 rad, one is getting an efficiency cut with the benefit of an about 20% higher conversion acceptance.

The leg distance is the second cut for background rejection. The leg distance should be small for conversions and is showing a maximum towards zero (see Fig. 4.17). The efficiency rises quickly in the first bins and is flattening afterwards (see Fig. 4.34). A purity cut can be applied for the upper limit of 0.01 cm with the trade-off of only 25% signal acceptance. The signal to background ratio is best for this cut position but the signal rejection is large. An efficiency cut can be applied at 0.1 cm which leads to about 95% acceptance for conversion-pairs.

The cosine of the pointing angle should also be small for γ-conversions and therefore produce a value near one. The efficiency of the conversions does also rise with decreasing speed from the maximum value to the more unlikely values. The behaviour is similar to the behaviour of the leg distance, but the signal-to-background ratio is slightly less significant. The variable can be used for purity purposes and produces the highest ratio value for a $\cos(\theta)$ of 0.999975.

The distance in the xy-plane (R) in Fig. 4.36 shows a significant difference

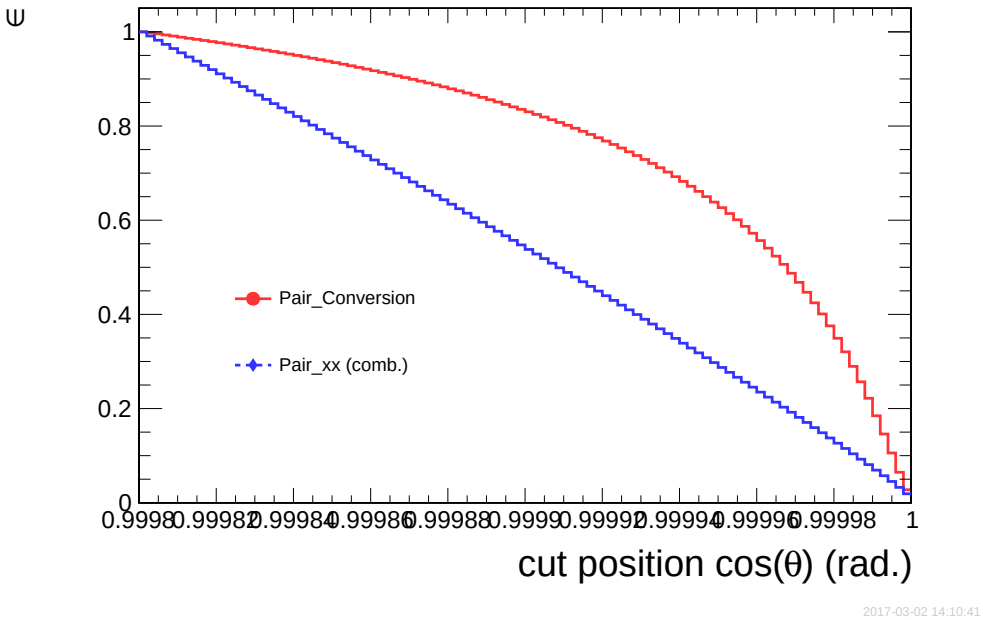

Figure 4.35: Signal efficiencies for the γ-conversions and the combinatorial background depending on the cut position of the cosine of the pointing angle.

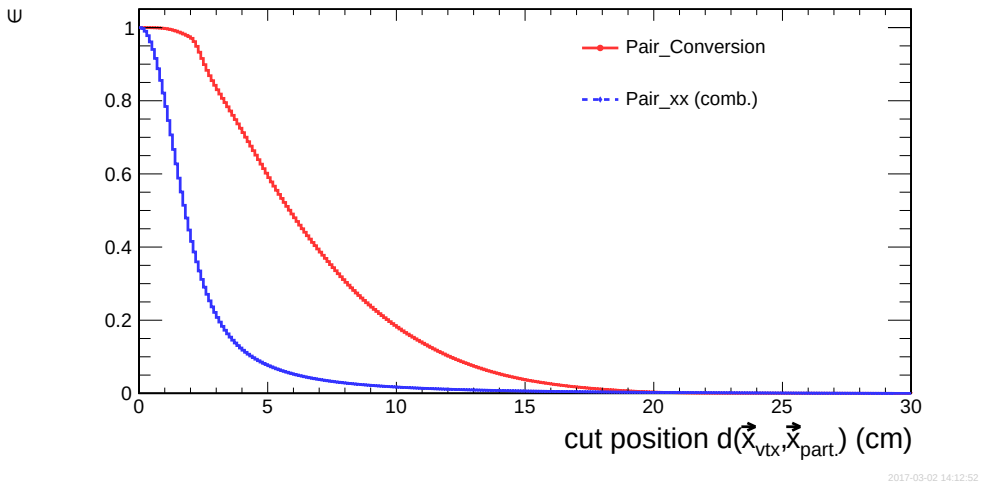

Figure 4.36: Signal efficiencies for the γ-conversions and the combinatorial background depending on the cut position of the distance in the xy-plane.

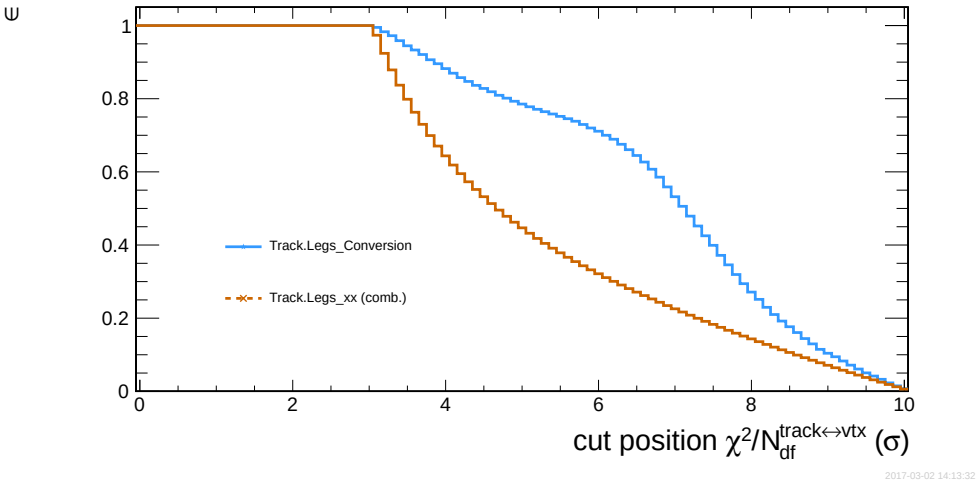

Figure 4.37: Signal efficiencies for the γ-conversions and the combinatorial background depending on the cut position of the χ^2/NDF to the vertex (track variable).

between the shapes of the conversions and the combinatorial background. Because of the comparably sharp maximum of the background one can use a lower cut to reject the background while maintaining the maximum of the conversions. A good ratio can be determined at the value of 2.2 cm.

Figure 4.37 shows the efficiency study for the χ^2 parameter for the tracks (see also Fig. 4.23). It is showing a strong rise for the signal around position of its maximum at the value 7.5 (see Fig. 4.23). For values below 6 the curve is flattening and the ratio is decreasing. Values below 3 are rejected by definition since these would lead to tracks which are pointing to the primary vertex and not the secondary vertex. To create purer electron samples a cut on the minimum value 6 can be applied.

The Armenteros-Podolanski plot was already mentioned in 4.2.3 to reduce the ambiguity between K^0_S and Λ. This can also be used to reject the kaon decays by an upper cut on the p_T^{arm} value. To reduce ambiguities between the conversion and the Λ and $\bar{\Lambda}$-decays due to smearing around the conversions' central position at the bottom of the plot a rejection cut via the armenteros ellipses of the Λ and $\bar{\Lambda}$ can be employed. To apply this cut for the Λ-decays one again has to use equation 4.5 to calculate the theoretical armenteros ellipses for the Λ and the $\bar{\Lambda}$ and vary the parameters to create a cutting region around the ideal ellipse.

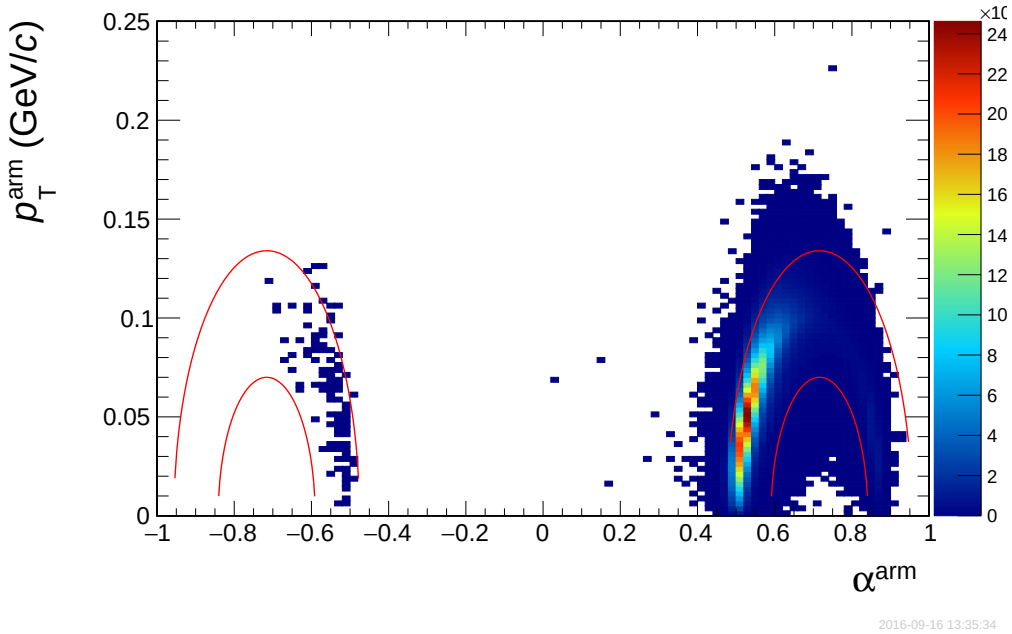

Figure 4.38: Armenteros-Podolanski plot for MC matched Λ and $\bar{\Lambda}$-decays and drawn with the Armenteros-Podolanski ellipse with variations in the used momenta and masses in equation 4.5.

Figure 4.38 is showing the result for the MC matched Λ and $\bar{\Lambda}$ signals. The amount $\bar{\Lambda}$ signals is very low so that the rejection of the $\bar{\Lambda}$ does not have a very large impact for this simulation analysis. The rejection of the Λ signals does not include all the widely distributed entries for the Λ, but it does include the clear majority. A further widening of the ellipse parameters would also effect the region of conversion entries.

The Φ_v variable is of special interest for the selection and rejection of conversions as it is displayed in Fig. 4.39. The γ-conversions are showing a sharp maximum around a value of 0.75 rad (see also Fig. 4.26). A local maximum does also exist for the other decays but it is far less significant and they are characterized by a wider distribution in general. A cut on the maximum value 1.0 produces sufficient results for the conversion selection.

Electron cut groups
With the information about the previously shown cut effects one can now separate the cut settings for the electron configuration into two sub-configurations,

one aiming at maximal purity and one optimizing the efficiency.

Cut group	Variable	Cut range
Efficiency cuts	opening angle	0.0-0.03 (rad.)
	leg distance	0.0-0.1 cm
	R	2.2-20
	chi^2/NDf to vtx	6.0-10.0
	Φ_v	0.0-1.3
	Armenteros kaon rejection	
	Armenteros lambda rejection	
Purity cuts	opening angle	0.0-0.01 (rad.)
	pointing angle	0.999975-1.0
	leg distance	0.0-0.01 cm
	R	2.2-20
	chi^2/NDf to vtx	6.0-10.0
	Φ_v	0.0-1.0
	Armenteros kaon rejection	
	Armenteros lambda rejection	

Figure 4.40 shows the resulting energy deposition distribution for the efficiency cut group and Fig. 4.41 shows the distribution of the purity cut group. Both distributions are momentum integrated and the solid red line is showing the sum of all accepted entries, while the dotted blue line is showing

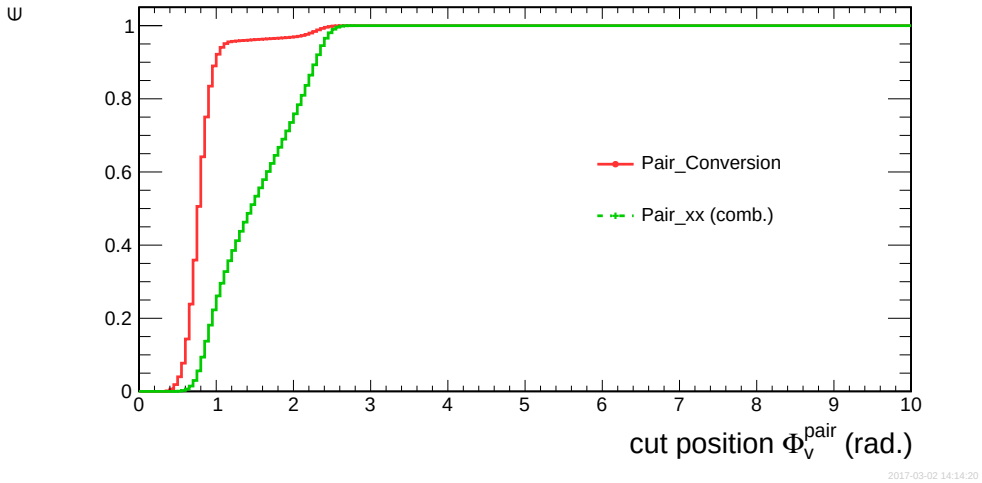

Figure 4.39: Signal efficiencies for the γ-conversions and the combinatorial background depending on the cut position of Φ_v.

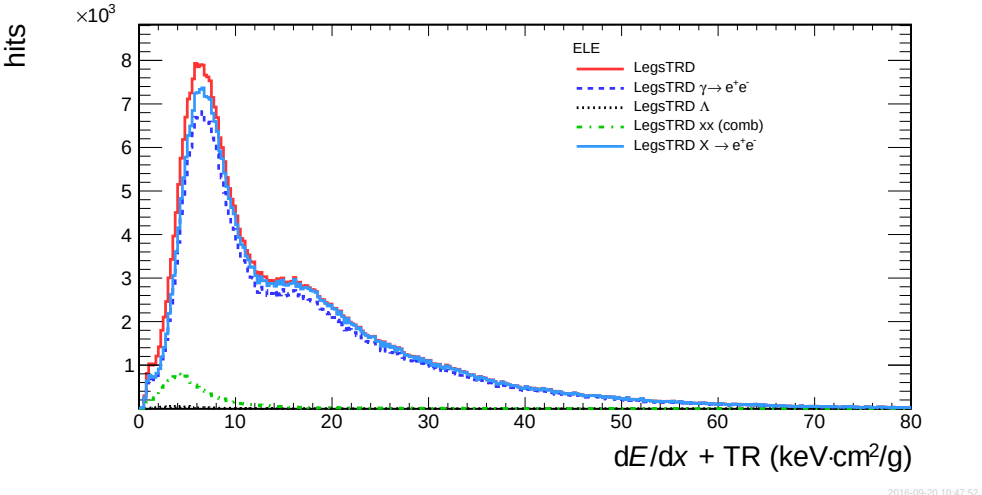

Figure 4.40: Energy deposition spectrum for electrons from γ-conversion selected through topology cuts of the efficiency cut group and identified with MC matching. The red line stands for the sum of all measurements and the X$\rightarrow$ e^+e^- are the combined values of electrons from conversions and electrons found into the xx background. The spectra are momentum integrated.

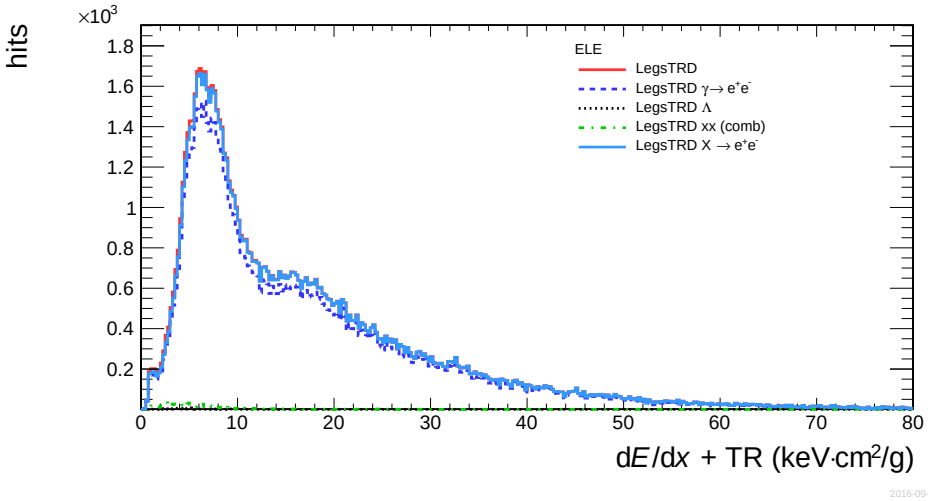

Figure 4.41: Energy deposition spectrum for electrons from γ-conversion selected through topology cuts of the purity cut group and identified with MC matching. The red line stands for the sum of all measurements and the X$\rightarrow e^+e^-$ are the combined values of electrons from conversions and electrons found into the xx background. The spectra are momentum integrated.

the electrons originating from γ-conversions and the solid blue line is also including other electron pairs which are found inside the combinatorial background (for example electron tracks which are mismatched as pairs). The dotted green line is showing the actual background which is still contaminating the electron sample.
In both cases there are no kaon-decays and practically no Λ and $\bar{\Lambda}$-decays. The amount of remaining background is not significant in the energy deposition spectrum of the purity cut group, but the efficiency group contains a low amount of remaining background which produces slight shifts in the low energy deposition region.
Also the spectrum of the purity cut group is showing fluctuations due to a low amount of statistics. In both cases the statistics is not sufficient to create momentum dependent likelihood probability distributions as in Fig. 4.11. This is also due to the practical computing restrictions of a simulation and the limited number of simulated events. A very careful approximation suggests the necessary time of data taking to produce a sufficient momentum dependent sample to be 327 h for the efficiency cuts and 1218 h for purity cuts (assuming an event rate of about 10 kHz minimum bias).

5 TRD performance studies

The last chapter of this work is designated to the analysis of some performance aspects of the CBM-TRD, in particular concerning the likelihood method for particle identification and its comparison to the artificial neural network.

Two crucial characteristics of the TRD are the electron identification efficiency and the related pion suppression. The electron identification efficiency is quantifying the amount of identified electrons in relation to the total amount of electrons. Therefore, it is the amount of electrons which are lost due to reconstruction and identification cuts.
Since the production rate of pions is a lot higher than the production rate of electrons, several detectors are needed to suppress a substantial part of the pions, because otherwise the pions would completely dominate the spectra and it would be very difficult to do any kind of electron analysis. The power of the pion suppression relies on the cut values used in the identification method and therefore is also correlated to the electron efficiency. The pion suppression is momentum dependent, since the different detectors are supposed to identify particles in different momentum regions. The most powerful momentum region for the CBM-TRD is above $p = 1$ GeV/c and especially in the region above 6 GeV/c where the RICH detector loses its suppression capabilities. In this momentum region the TRD is absolutely necessary. Above a momentum of $p = 6$ GeV/c the RICH can not identify the particles any more. From that point the pion suppression has to be provided by the TRD. Figures 5.1 and 5.2 show the pion suppression factor with the TRD adjusted to 80% electron identification efficiency with the likelihood method in Fig. 5.1 and the ANN in Fig. 5.2. Both Figures show that the TRD is enhancing the pion suppression in the low momentum region, too. In the higher momentum region the pion suppression is basically achieved by the TRD alone. The comparison between the likelihood method and the ANN shows that the results of both identification methods are very similar. The corresponding electron identification efficiency is shown in Fig. 5.3.

As mentioned before, the pion suppression depends on the electron identification efficiency since stricter identification cuts produce a lower identification uncertainty and therefore exclude more pions. The trade-off for the better identification is lower statistics. Figs. 5.4 and 5.5 show the pion suppression factors for the different detector configurations at 70% and 90% electron efficiency, as a function of momentum. A lower electron identification efficiency increases the pion suppression factor but reduces the statistics.

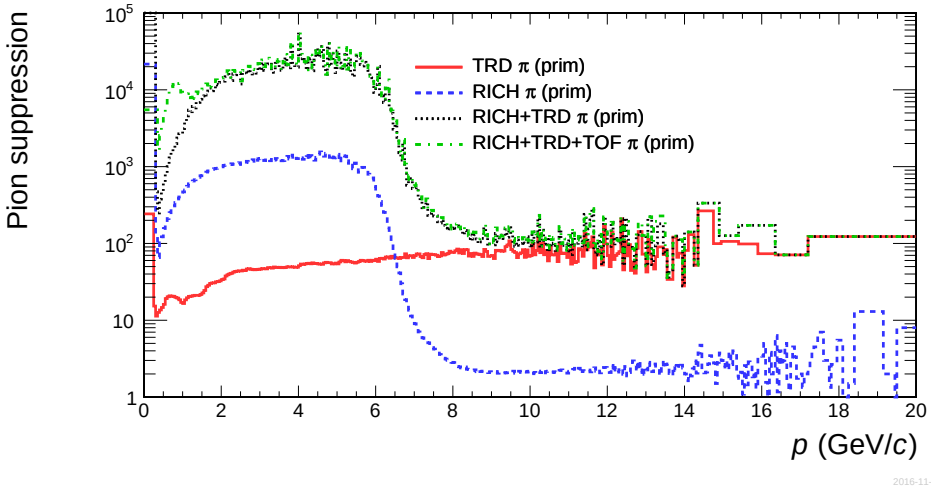

Figure 5.1: Comparison of the pion suppression factors obtained with the likelihood method for different detector configurations at an electron identification efficiency of 80% for the TRD.

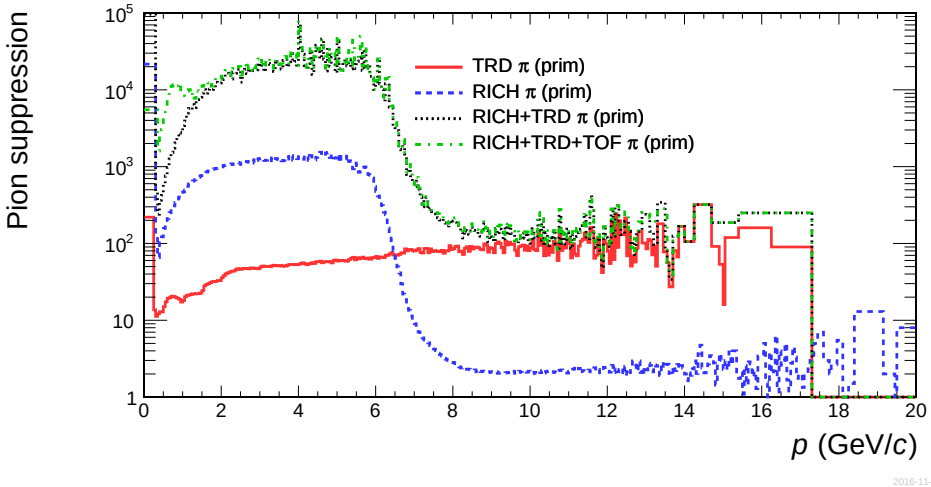

Figure 5.2: Comparison of the pion suppression factors obtained with the ANN for different detector configurations at an electron identification efficiency of 80% for the TRD.

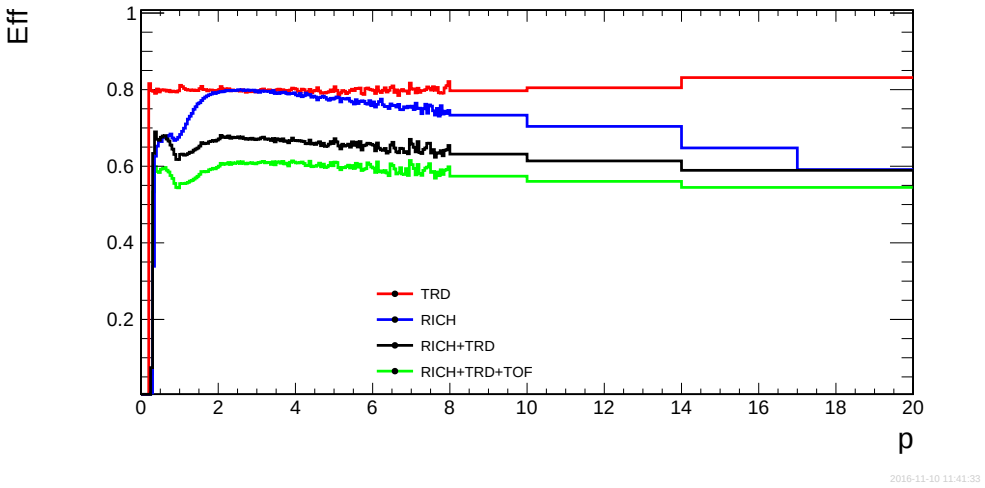

Figure 5.3: Electron identification efficiencies for the likelihood method.

With these information one can now further investigate the behaviour of different decays into di-electrons. Here, one has to take the branching ratios and expected yields into account [F.] [T. 16b] [W.]:

Source	$BR_{e^+e^-}$	Total multiplicities (Au+Au) central 10% 8 A GeV
ρ^0	$4.72 \cdot 10^{-5}$	9.0
ω	$7.28 \cdot 10^{-4}$	19.0
ϕ	$2.97 \cdot 10^{-4}$	0.12
In-medium radiation		$2.2 \cdot 10^{-2}$
QGP radiation		$5.8 \cdot 10^{-3}$

The resulting invariant mass distributions are shown in Figs. 5.6 and 5.7. For the RICH detector the ANN is used for PID, which has been adjusted to a momentum dependent electron identification efficiency around 90% average. For the TRD the likelihood method with momentum independent

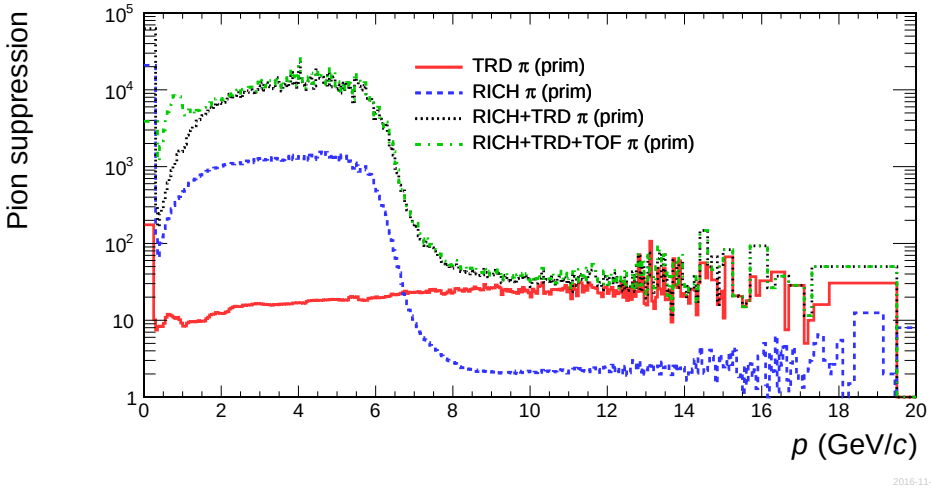

Figure 5.4: Pion suppression factors for different detector configurations obtained with the likelihood method and adjusted to an electron identification efficiency of 90%.

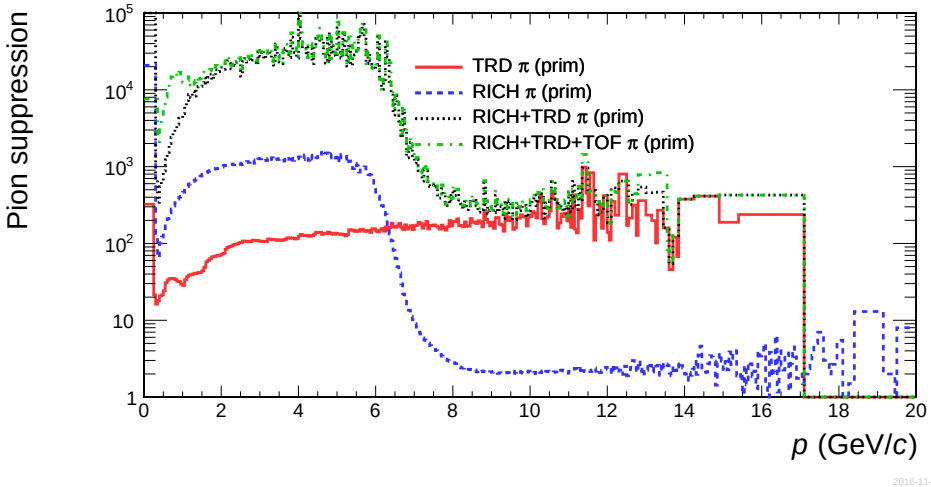

Figure 5.5: Pion suppression factors for different detector configurations obtained with the likelihood method and adjusted to an electron identification efficiency of 70%.

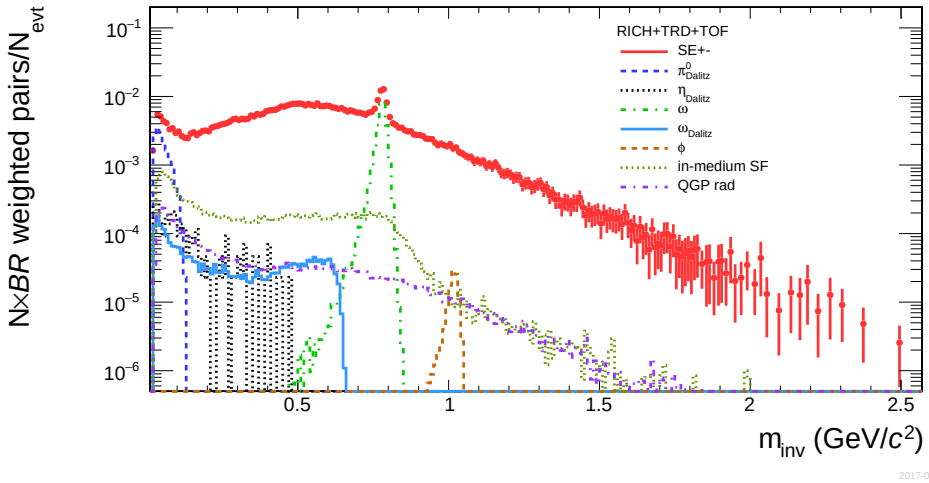

Figure 5.6: Invariant mass distributions for various unlike-sign electron pairs for central (10%) Au+Au collisions at 8 A GeV. All contributions are weighted with their expected yield and their branching ratio. The electron identification has been performed with the likelihood method, adjusted to 80% electron efficiency in the TRD.

80% electron efficiency has been employed. The signals were simulated for Au+Au collisions at 8 A GeV for central (10%) events.

Figure 5.7 shows the large fraction of combinatorial di-electrons in comparison to the total amount of pairs. The two most significant background contributions are the di-electron (ee) and the electron-pion ($e\pi$) channels. Their yields are influenced by the electron identification efficiency and the pion suppression. In the region of invariant masses between m_{inv}= 1.5 - 2.5 GeV/c^2 the relative contribution of the $e\pi$ channel to the total amount reconstructed unlike-sign pairs increases. This leads to the signal-to-background ratio shown in Fig. 5.10 (black line). There are two local maxima at the positions of the ω and in the lower invariant mass region for the mixture of Dalitz decays. The invariant mass range above m_{inv}= 1.5 GeV/c^2 has a signal-to-background ratio larger than 10^{-2}, which is expected to be a sufficient value to provide experimental access to thermal radiation.

Figures 5.8 and 5.9 show the same invariant mass spectra, but without the usage of the TRD. Fig. 5.8 shows that the relative contribution of the di-electron signals to the total amount of reconstructed unlike-sign pairs decreases, while Fig. 5.9 shows an dramatic increase of the background signals.

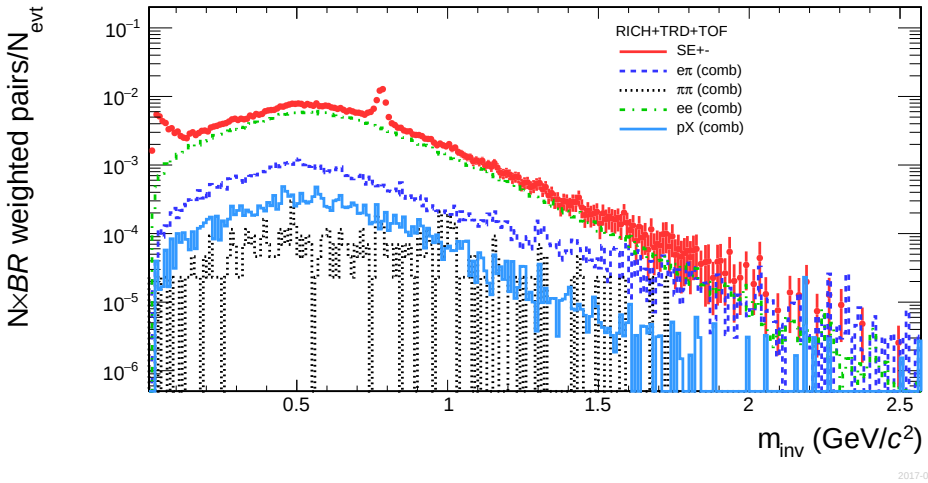

Figure 5.7: Invariant mass distributions for different combinatorial background contributions at 8 A GeV central (10%) Au+Au collisions. All contributions are weighted with their expected yield and their branching ratio. The electron identification has been performed with the likelihood method, adjusted to 80% electron efficiency in the TRD.

Due to the much lower pion suppression, the contributions that include a pion increase drastically. Especially in the invariant mass region above m_{inv} = 1.5 GeV/c^2 the background is dominated by the $e\pi$ and the $\pi\pi$ contribution. The $\pi\pi$ contribution depends on the pion suppression squared and therefore is strongly suppressed when using the TRD, while it is dominant for higher invariant masses without a TRD. The resulting signal-to-background ratio is shown in Fig. 5.10 (red line). The ratio without the TRD has smaller values for all invariant masses and for invariant masses above m_{inv}= 1.5 GeV/c^2 it is decreasing to values below 10^{-3}, which is nearly two orders of magnitude lower than with the TRD.

Further information on the impact of the electron identification efficiency and the corresponding pion suppression can be gained from the comparison between the invariant mass spectra of the background for 70% and 90% electron identification efficiency (see Figs. 5.11 and 5.12). The yield of all background contributions decreases with a lower efficiency, but the channels that include a π are particularly affected, since they depend on the pion suppression factor, which changes by a large amount. The $e\pi$ channel has the largest fraction of the reconstructed pairs at invariant masses above m_{inv} = 1.5 GeV/c^2 at an efficiency of 90%. The ee channel is not affected as much,

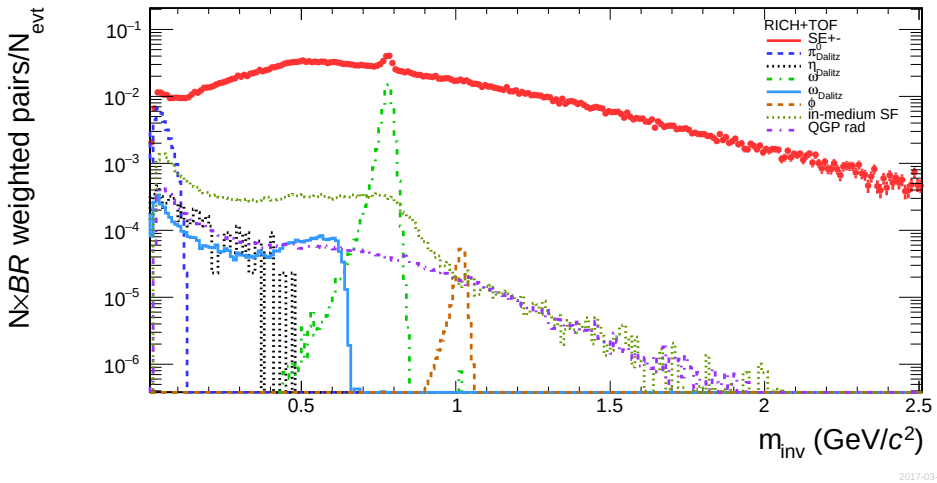

Figure 5.8: Invariant mass distribution for various unlike-sign electron pairs for central (10%) Au+Au collisions at 8 A GeV determined without a TRD. All contributions are weighted with their expected yield and their branching ratio.

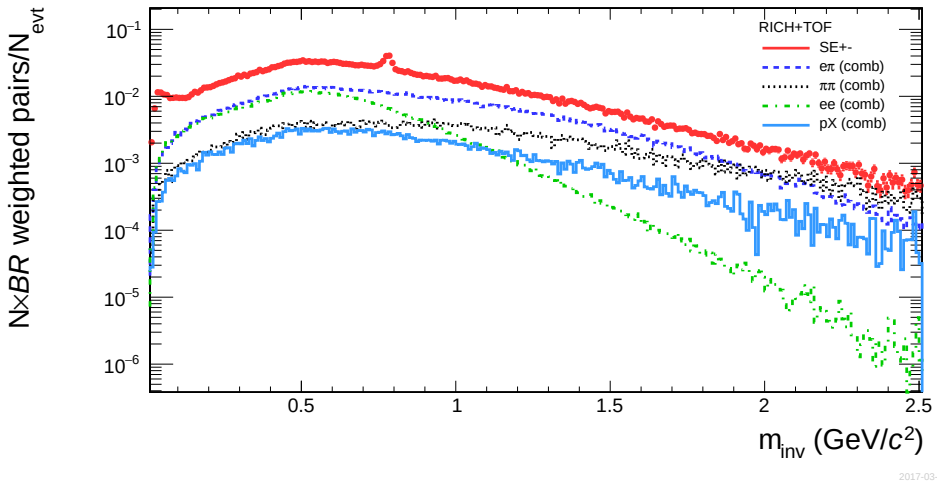

Figure 5.9: Invariant mass distribution for different pair background contributions for central (10%) Au+Au collisions at 8 A GeV determined without a TRD. All contributions are weighted with their expected yield and their branching ratio.

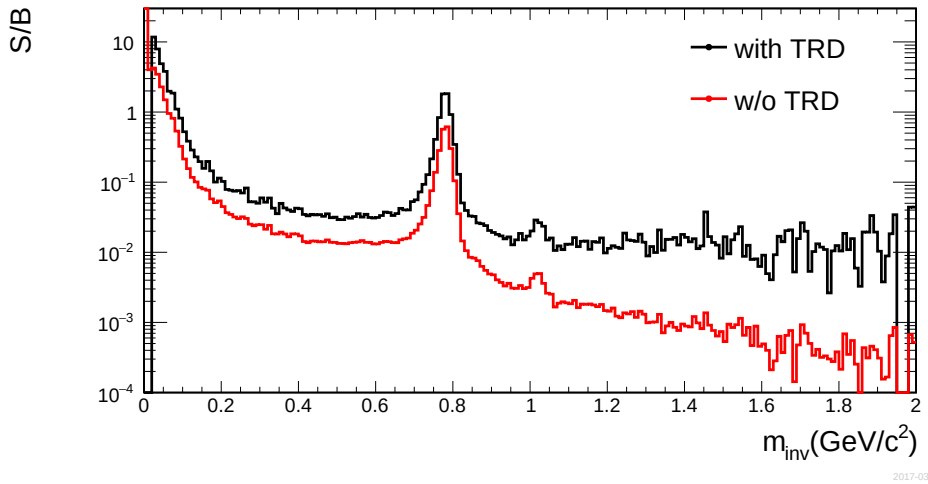

Figure 5.10: Signal-to-background ratio as a function of the invariant mass for different signals at 8 A GeV central (10%) Au+Au collisions. All contributions are weighted with their expected yield and their branching ratio. The electron identification has been performed with the likelihood method, adjusted to 80% electron efficiency in the TRD for the black line.

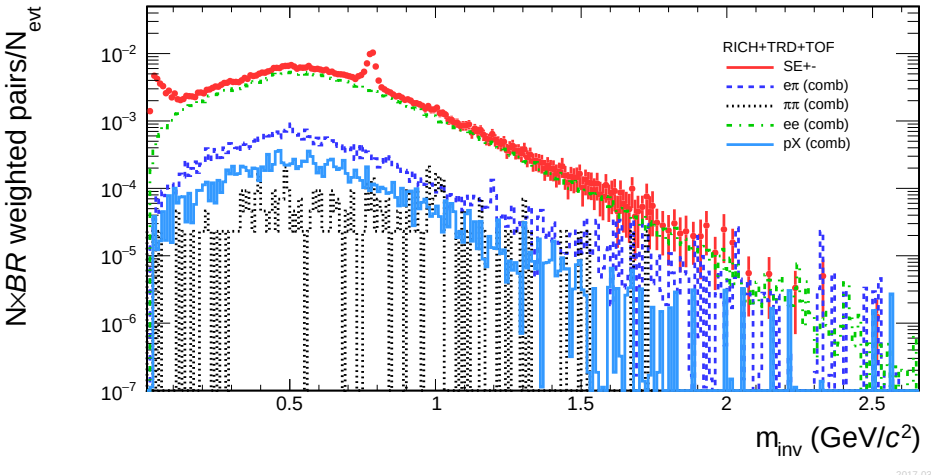

Figure 5.11: Invariant mass distribution for different pair background contributions for central (10%) Au+Au collisions at 8 A GeV. All contributions are weighted with their expected yield and their branching ratio. The electron identification has been performed with the likelihood method, adjusted to 70% electron efficiency in the TRD.

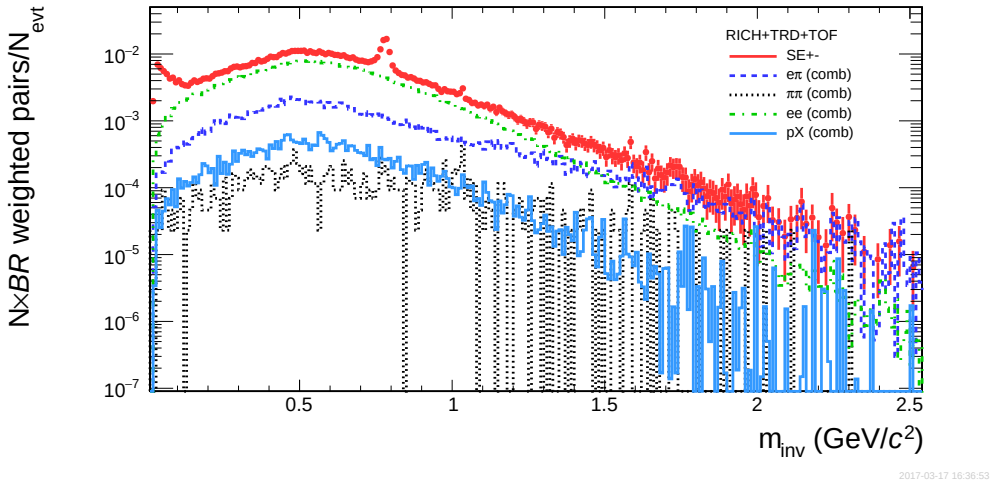

Figure 5.12: Invariant mass distribution for different pair background contributions for central (10%) Au+Au collisions at 8 A GeV. All contributions are weighted with their expected yield and their branching ratio. The electron identification has been performed with the likelihood method, adjusted to 90% electron efficiency in the TRD.

since it only depends on the direct influence of the electron efficiency.

Since we are especially interested in the invariant mass region above 1.5 GeV/c^2, the effects of different electron identification efficiencies on the background contributions ee, $e\pi$, $\pi\pi$ and the thermal in-medium+QGP radiation shall be investigated further. To arrive at more quantitative conclusions a closer look at the integrated yields of the combinatorial background in the invariant mass region of m_{inv}=1.5-2.5 GeV/c^2 can be seen in Fig. 5.13. Again, the results are showing the direct influence of the electron efficiency on the electron contributions and the stronger influence of the pion suppression on the yields of the background π contributions. The $e\pi$ contributions in Fig. 5.13 show an increase of about a factor 10 between 70% and 90% and has a larger total contribution than the ee channel for 90% efficiency. The $\pi\pi$ contributions are increasing by the same amount, but they are not yet dominating the investigated invariant mass range.
The contributions of $e\pi$ in comparison to ee can also be displayed via the crossing point of the ee and the $e\pi$ contributions which is shown in Fig. 5.14. The crossing point is defined as the invariant mass value where the ee and the $e\pi$ contributions produce the same yield. The point is moving towards higher invariant masses as the efficiency decreases, which indicates a higher

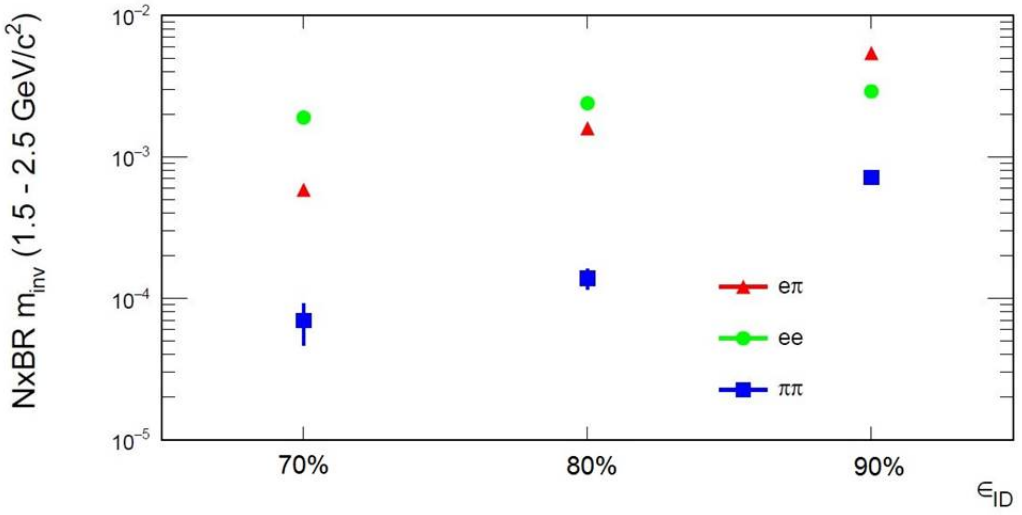

Figure 5.13: Integrated yield for background pair combinatorics in the invariant mass range of 1.5 - 2.5 GeV/c^2.

pion suppression factor and also will provide a better access to the radiation signals.
A closer look into the signal-to-background ratio of the mixture of the thermal in-medium and QGP radiation in comparison to the background shows the effects of the previous observations. Figure 5.15) shows an increasing difference between the efficiency settings towards higher invariant masses, which is due to the larger impact of pion suppression of the TRD on the π contributions in the invariant mass range above $m_{inv} = 1.5$ GeV/c^2. There are large fluctuations for invariant masses above $m_{inv} = 2.0$ GeV/c^2, because of the low statistics in this region.

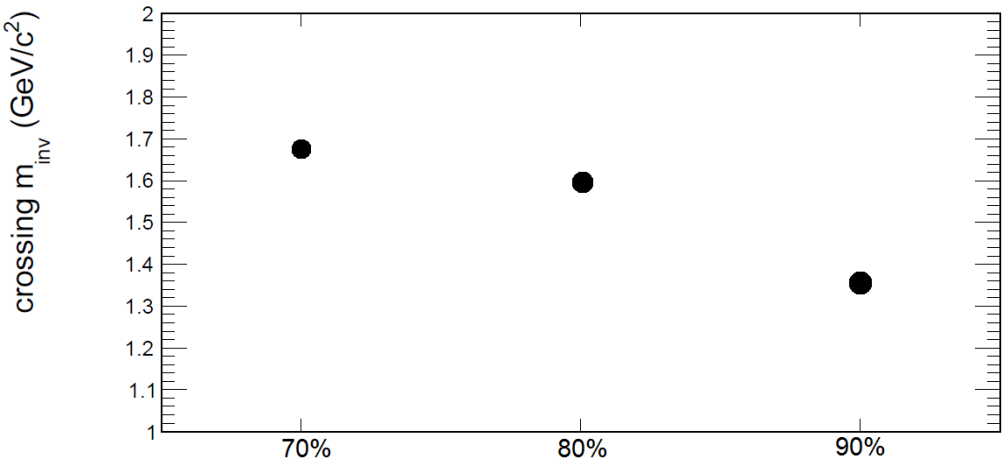

Figure 5.14: Crossing point of the ee and the $e\pi$ contribution as a function of the electron identification efficiency

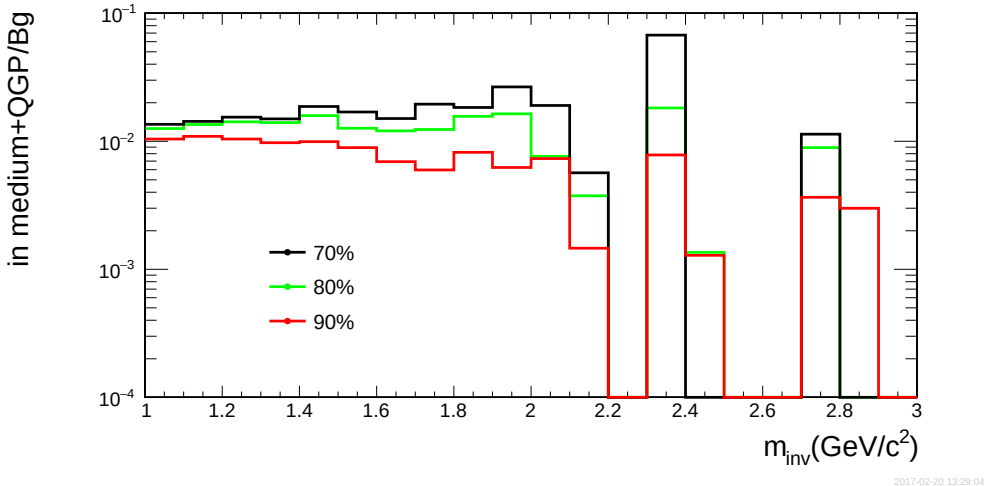

Figure 5.15: Signal-to-background ratio for different efficiencies in the invariant mass range of m_{inv}=1.0-3.0 GeV/c^2

6 Summary

In this work a likelihood method has been implemented and investigated as particle identification algorithm for the CBM-TRD.

The creation of the probability distributions for the likelihood method via V0-topologies seems to be feasible and the purity of the obtained samples is sufficient for the usage in the likelihood method.

The comparison between the ANN and the likelihood method shows no differences in the identification performance. The pion suppression factor reaches the same values for the same electron identification efficiencies and the yields of the resulting di-lepton signals are comparable. The signal-to-background ratios for both methods have the same values and show a value of about 10^{-2} in the invariant mass range of m_{inv} = 1.5 - 2.5 GeV/c^2, which is expected to be sufficient to provide access to the thermal in-medium and QGP radiation.

The investigation of a detector system without a TRD shows no pion suppression for a momentum above p = 6 GeV/c. Therefore, the background contributions increase drastically and the signal-to-background ratio decreases at all invariant masses, but especially in the invariant mass range of m_{inv} = 1.5 - 2.5 GeV/c^2.

The background contributions in the invariant mass range of m_{inv} = 1.5 - 2.5 GeV/c^2 are also influenced by the selected electron identification efficiency of the TRD, which significantly shifts the fraction of the $e\pi$ contributions relative to the total number of pairs.

7 Danksagung

Zuerst möchte ich Christoph Blume danken für die Möglichkeit in seiner Gruppe zu arbeiten und bei ihm diese Arbeit zu verfassen. Er ermutigt seine Studenten stets ihre Arbeit zu präsentieren und mit ihren Forschungen weiter zu machen.
Als nächtes möchte ich Julian Book danken, der die meiste Zeit mein Betreuer war und mir dabei eine Menge über die Arbeit in der Hochenergiephysik beigebracht hat.
Natürlich danke ich auch der restlichen Arbeitsgruppe, die immer eine sehr angenehme Arbeitsatmospähre erzeugt hat.

Ich danke auch nochmal speziell Max Zutschke, mit dem ich mich schon immer gut über die Programmierung und die Physik austauschen konnte und der mich dabei in meiner Arbeit ungemein unterstützt hat.

Zuletzt danke ich auch meiner Familie, die mich in meinem ganzen Studium unterstützt hat und es mir damit überhaupt erst ermöglicht hat.

References

[AAI+07] EP Akishina, TP Akishina, VV Ivanov, AI Maevskaya, and OA Afanas' ev. Electron/pion identification in the cbm trd using a multilayer perceptron. *JINR Communication E10-2007-17. Dubna*, 2007.

[All80] Allison, WWM and Cobb, JH. Relativistic charged particle identification by energy loss. *Annual Review of Nuclear and Particle Science*, 30(1):253–298, 1980.

[And11] Andronic A. and Wessels J.P. Transition Radiation Detectors. https://arxiv.org/abs/1111.4188, 2011.

[APP] APPA. {http://www.fair-center.eu/public/experiment-program/appa-physics.html}. [Online; accessed 30-November-2016].

[Are14] Andreas Arend. *Optimization of a Transition Radiation Detector for the Compressed Baryonic Matter Experiment* . PhD thesis, 12 2014.

[ATL12] ATLAS Collaboration, CMS Collaboration. Combined Measurement of the Higgs Boson Mass in pp Collisions at $\sqrt{s}$=7 and 8 TeV with the ATLAS and CMS Experiments. *Phys. Rev. Lett. 114, 191803*, 2012.

[AW12] A. Andronic and J.P. Wessels. Transition radiation detectors. *Nuclear Instruments and Methods in Physics Research Section A: Accelerators, Spectrometers, Detectors and Associated Equipment*, 666:130 – 147, 2012. Advanced Instrumentation.

[BF09] J.Knoll S. Leupold J. Randrup R.Rapp P. Senger B. Friman, C. Höhne. CBM-Physics Book. pages 863–878, Sep 2009.

[Blu16] C. Blume. Gasdetektoren. https://elearning.physik.uni-frankfurt.de/goto_FB13-PhysikOnline_file_11987_download.html, 2016. [Online; accessed 15-December-2016].

[CHMP74] Michael L. Cherry, Gernot Hartmann, Dietrich Müller, and Thomas A. Prince. Transition radiation from relativistic electrons in periodic radiators. *Phys. Rev. D*, 10:3594–3607, Dec 1974.

[Chr17] Christian S. Fischer. Deconfinement phase transition and the quark condensate. {http://www.thphys.uni-heidelberg.de/~smp/view/SeminarTalks/fischer.pdf}, 2017. [Online; accessed 19-January-2017].

[Cyr09] Bergmann Cyrano. Development and Test of a Transition Radiation Detector Prototype for CBM @ FAIR . https://www.gsi.de/documents/DOC-2010-Apr-181.html, 2009.

[ea04] A. Andronic et al. Energy loss of pions and electrons of 1 to 6 gev/c in drift chambers operated with xe,co2(15%). *Nuclear Instruments and Methods in Physics Research Section A: Accelerators, Spectrometers, Detectors and Associated Equipment*, 519(3):508 – 517, 2004.

[ea14] P. P. Bhaduri et al. *Phys. Rev.*, C 89:044912, 2014.

[F.] F. Seck et al. Development of a Realistic Event Generator for In-Medium and QGP Dileptons.

[Fai] Fair Project. {https://www.gsi.de/forschungbeschleuniger/fair.htm}. [Online; accessed 30-November-2016].

[Gal09] T. Galatyuk. *Di-electron spectroscopy in HADES and CBM: from p + p and n + p collisions at GSI to Au + Au collisions at FAIR.* PhD thesis, 2009.

[Gal14] T. Galatyuk. HADES overview. *Nucl. Phys.*, A931::41–51, 2014.

[H. 10] H. J. Specht. *AIP Conf. Proc.* , 1322:1, 2010.

[I. 07] I. Froehlich et al. *PoS(ACAT2007)*, 076, 2007.

[Mic16] Michael Nielsen. Neural networks. {http://neuralnetworksanddeeplearning.com/chap1.html}, 2016. [Online; accessed 28-November-2016].

[MS86] T. Matsui and H. Satz. J/Ψ suppression by quark-gluon plasma formation. *Physics Letters B*, 178(4):416 – 422, 1986.

[NUS] NUSTAR. {http://www.fair-center.eu/public/experiment-program/nustar-physics.html}. [Online; accessed 30-November-2016].

[PAN] PANDA. {http://www.fair-center.eu/public/experiment-program/antiproton-physics/panda.htmll}. [Online; accessed 30-November-2016].

[Par16] Particle data group. Particle listing. {http://www-pdg.lbl.gov/2016/html/computer_read.html}, 2016.

[Pica] Pic. Fundamental forces. {http://ictwiki.iitk.ernet.in/wiki/images/thumb/Chapter_17_figure_1.png/550px-Chapter_17_figure_1.png}. [Online; accessed 23-November-2016].

[Picb] Pic. Gluonenzustände. {https://upload.wikimedia.org/math/7/3/3/733d1e87292418fcb90eab652a3508b0.png}. [Online; accessed 07-August-2015].

[Picc] Pic. Strong coupling. {https://upload.wikimedia.org/wikipedia/commons/thumb/8/81/Strong_coupling_as_function_of_energy.svg/220px-Strong_coupling_as_function_of_energy.svg.png}. [Online; accessed 07-August-2015].

[Picd] Pic. The standard model. {https://upload.wikimedia.org/wikipedia/commons/thumb/0/00/Standard_Model_of_Elementary_Particles.svg/375px-Standard_Model_of_Elementary_Particles.svg.png}. [Online; accessed 07-August-2015].

[R. 99] R. Rapp and J.Wambach. *Eur. Phys. J.*., A 6:415555, 1999.

[rut17] Rutherford model of the atom. {http://www.iun.edu/~cpanhd/C101webnotes/modern-atomic-theory/rutherford-model.html}, 2017.

[RvH16] R. Rapp and H. van Hees. Thermal Dileptons as Fireball Thermometer and Chronometer. *Phys. Lett.*, B:753:586–590, 2016.

[sta17] The standard model of particle physics. {http://www.benbest.com/science/standard.html}, 2017.

[str17] Introduction to QCD and the standard model. {http://www.physics.umd.edu/courses/Phys741/xji/chapter1.pdf}, 2017.

[T. 16a] T. Ablyazimov et al. Challenges in QCD matter physics - The scientific programme of the Compressed Baryonic Matter experiment at FAIR. *CBM report*, pages 9–10, 2016.

[T. 16b] T. Galatyuk. *Eur. Phys. J..*, A 52:131, 2016.

[tho17] Thomson model of the atom. {https://en.wikipedia.org/wiki/Plum_pudding_model}, 2017.

[TR] Transition radiation. {http://www.kph.uni-mainz.de/Illustrationen/w_x1_1.jpg}. [Online; accessed 01-December-2016].

[W.] W. Cassing et al. *Nucl Phys A691 (2001) 753.*

[Wen08] Marc Wengenroth. Charakterisierung von kryogenen sorptionsflächen im variablen temperaturbereich zwischen 10-50 k für das sis 100/300, 2008.

[wg16] The TRD working group. Technical Design Report for the CBM - Transition Radiation Detector (In preparation). 2016.

8 Eidesstattliche Erklärung

Ich erkläre hiermit, dass ich die vorliegende Arbeit selbständig und ohne Benutzung anderer als der angegebenen Hilfsmittel angefertigt habe; die aus fremden Quellen direkt oder indirekt übernommenen Gedanken sind ausnahmslos als solche kenntlich gemacht. Ferner erkläre ich,dass ich die Arbeit nicht -auch nicht auszugsweise- Für eine andere Prüfung verwendet wurde.

Frankfurt, der 23.03.2017

Etienne Bechtel